DOT/FAA/TC-13/31

Federal Aviation Administration
William J. Hughes Technical Center
Aviation Research Division
Atlantic City International Airport
New Jersey 08405

Computational Flame Characterization of New Large Aircraft Immersed in Hydrocarbon Pool Fires

August 2013

Final Report

This document is available to the U.S. public through the National Technical Information Services (NTIS), Springfield, Virginia 22161.

This document is also available from the Federal Aviation Administration William J. Hughes Technical Center at actlibrary.tc.faa.gov

U.S. Department of Transportation
Federal Aviation Administration

NOTICE

This document is disseminated under the sponsorship of the U.S. Department of Transportation in the interest of information exchange. The United States Government assumes no liability for the contents or use thereof. The United States Government does not endorse products or manufacturers. Trade or manufacturer's names appear herein solely because they are considered essential to the objective of this report. The findings and conclusions in this report are those of the author(s) and do not necessarily represent the views of the funding agency. This document does not constitute FAA policy. Consult the FAA sponsoring organization listed on the Technical Documentation page as to its use.

This report is available at the Federal Aviation Administration William J. Hughes Technical Center's Full-Text Technical Reports page: actlibrary.tc.faa.gov in Adobe Acrobat portable document format (PDF).

Technical Report Documentation Page

1. Report No.	2. Government Accession No.	3. Recipient's Catalog No.
DOT/FAA/TC-13/31		

4. Title and Subtitle	5. Report Date
COMPUTATIONAL FLAME CHARACTERIZATION OF NEW LARGE AIRCRAFT IMMERSED IN HYDROCARBON POOL FIRES	August 2013
	6. Performing Organization Code
7. Author(s) Christopher P. Menchini	8. Performing Organization Report No.
9. Performing Organization Name and Address U.S. Air Force Research Laboratory (AFRL) Materials and Manufacturing Directorate Airbase Technologies Division 139 Barnes Drive, Suite 2 Tyndall AFB Panama City, FL 32403 Christopher P. Menchini Applied Research Associates 421 Oak Avenue Panama City, FL 32401	10. Work Unit No. (TRAIS)
	11. Contract or Grant No. DTFACT-06-X-0007
12. Sponsoring Agency Name and Address Federal Aviation Administration Airport Safety and Operations Division (AAS-300) 800 Independence Avenue SW Washington, DC 20591	13. Type of Report and Period Covered Final Report
	14. Sponsoring Agency Code AAS-300

15. Supplementary Notes

The Federal Aviation Administration Airport and Aircraft Safety R&D Division COR was Keith Bagot.

16. Abstract

New Large Aircraft (NLA) pose unique firefighting challenges unique for traditional aircraft. Specifically, questions have arisen regarding the applicability of current firefighting protection standards to nonconventional design changes, such as fuselage shape modifications, enhanced material compositions, new fuel storage locations, and unique passenger loading configurations. To address fuselage shape concerns, a computational fluid dynamic (CFD) modeling strategy was developed to quantify heat transfer to the aircraft for a given aircraft geometry and hydrocarbon pool fire condition. The CFD predictions supported experimental validation data conclusions showing increased crosswinds amplify heat transfer to the aircraft surface due to enhanced turbulent fuel-air mixing. Based upon the predicted CFD fire plume structure and aircraft surface heat transfer magnitudes, nominal changes in aircraft geometry exposed to similar scale flame and atmospheric conditions pose no extraordinary firefighting challenge. All thermal attributes stayed within the same order of magnitude and, in the majority of instances, varied less than 15%.

17. Key Words	18. Distribution Statement
New Large Aircraft (NLA), Firefighting, Aircraft Rescue and Firefighting (ARFF), Computational fluid dynamic (CFD), Discrete ordinates, Differential pressure gage, Heat flux gage, Practical critical area (PCA), Reynolds number, Turbulence intensity	This document is available to the U.S. public through the National Technical Information Service (NTIS), Springfield, Virginia 22161. This document is also available from the Federal Aviation Administration William J. Hughes Technical Center at actlibrary.tc.faa.gov

19. Security Classif. (of this report)	20. Security Classif. (of this page)	21. No. of Pages	22. Price
Unclassified	Unclassified	57	

Form DOT F 1700.7 (8-72) Reproduction of completed page authorized

TABLE OF CONTENTS

			Page
EXECUTIVE SUMMARY			xi
1.	INTRODUCTION		1
	1.1	Background	1
	1.2	Scope	2
2.	LITERATURE REVIEW		3
	2.1	Overview	3
	2.2	Physical Characteristics of Large-Scale Pool Fires	3
	2.3	Objects Immersed in Large-Scale Pool Fires	4
	2.4	Large-Scale Pool Fire Modeling	5
3.	COMPUTATIONAL MODEL VALIDATION		6
	3.1	Overview	6
	3.2	Experimental Summary	7
	3.3	Computational Model Setup	9
		3.3.1 Turbulence	10
		3.3.2 Combustion	10
		3.3.3 Radiation Heat Transfer	11
		3.3.4 Soot Formation	12
		3.3.5 Physical Flow Domain	12
		3.3.6 Boundary Conditions	14
		3.3.7 Numerics	15
	3.4	Results	15
		3.4.1 Surface Pressures	15
		3.4.2 Flame Temperatures	18
		3.4.3 Surface Temperatures	22
		3.4.4 Surface Heat Fluxes	24
		3.4.5 Flow Visualization	26
4.	AIRCRAFT COMPUTATIONAL ANALYSIS		27
	4.1	Overview	27
	4.2	Physical Domain	29
	4.3	Boundary Conditions	30
	4.4	Results	30

4.4.1 Surface Temperatures and Heat Fluxes 31
4.4.2 Flame Temperatures 38
4.4.3 Flame Velocities 40

5. CONCLUSIONS 41

6. REFERENCES 42

LIST OF FIGURES

Figure		Page
1	The NLA A380 in Relative Size Comparison to the B-747-400 and a Composite Profile Map of the A380	1
2	The NLA Mockup Engulfed in a JP-8 Pool Fire and After the JP-8 Pool Fire Using Infrared Imagery	2
3	The Experimental Set-up Showing the C-141 Mock Fuselage in a 20-m-Diameter Fuel Pit and an Overhead Schematic With Approximate DPG, HFG, and TC Locations	8
4	Adapted Instantaneous Screen Capture of the Mock Fuselage Fully Engulfed in Fire Exposed to a Medium Wind Condition and a Time-Averaged Video of the Same Conditions	9
5	Comparison of Physical and Chemical Combustion Time-Scales	11
6	Experimental Validation Case Showing a Near-Field View of the Relative Dimensions of the Fuel Pool and Mock Fuselage and an Isometric View of the Equivalent Geometric Surface Mesh	13
7	Experimental Validation Case Geometric Mesh	13
8	Far-Field Schematic Outlining CFD Boundary Types and Conditions	14
9	Near-Field Schematic Outlining CFD Boundary Types and Conditions	15
10	Medium Wind Condition Transient Experimental DPG Measurements on the Mock Fuselage Compared to Time-Averaged Steady CFD Results	16
11	The CFD Static Pressure Calculated About the Mock Fuselage Cylinder	17
12	Centerline CFD Mock Fuselage Near-Field Total Pressure Contours of the Medium Wind Condition	17
13	The CFD Mock Fuselage Near-Field Velocity Magnitude Vectors of the Medium Wind Condition	18
14	Low Crosswind Case Showing Flame Temperature Contour Comparisons	20
15	Medium Crosswind Case Showing Flame Temperature Contour Comparisons	21
16	High Crosswind Case Showing Flame Temperature Contour Comparisons	22
17	Low Crosswind Case Showing Mock Fuselage Surface Temperature Contours Comparisons	23

18	Medium Crosswind Case Showing Mock Fuselage Surface Temperature Contour Comparisons	23
19	High Crosswind Case Showing Mock Fuselage Surface Temperature Contour Comparisons	24
20	Low Crosswind Case Showing Mock Fuselage Surface Heat Flux Contour Comparisons	25
21	Medium Crosswind Case Showing Mock Fuselage Surface Heat Flux Contour Comparisons	25
22	High Crosswind Case Showing Mock Fuselage Surface Heat Flux Contour Comparisons	26
23	Flame and Surface Contour Temperatures for the Case CFD Validation Case Studies	26
24	The PCA Size and Location With Respect to the Aircraft	27
25	A Comparison of the Relative Scale and Shape Between Each Aircraft	28
26	An Alternative Perspective Comparing the Relative Scale and Shape Between Each Aircraft	29
27	The A380 Geometric Mesh	30
28	Comparisons of Mean Aircraft Surface CFD Temperatures and Heat Fluxes Exposed to Low and Medium Crosswinds	31
29	Top View of Time-Averaged Aircraft Surface Temperatures Exposed to Medium Crosswinds	33
30	Bottom View of Time-Averaged Aircraft Surface Temperatures Exposed to Medium Crosswinds	34
31	Top View of Time-Averaged Aircraft Surface Heat Flux Exposed to Medium Crosswinds	35
32	Bottom View of Time-Averaged Aircraft Surface Heat Flux Exposed to Medium Crosswinds	36
33	Time-Averaged Near-Field Aircraft Surface Fuel Zone and Ground Temperatures Exposed to Medium Crosswinds (Isometric View)	37
34	Time-Averaged Near-Field Ground and Fuel Surface Temperatures Exposed to Medium Crosswinds (Top View)	38
35	Time-Averaged Far-Field Fire Plume Temperatures Exposed to Medium Crosswinds (Front View)	39

36 Time-Averaged Near-Field Fire Plume Temperatures Exposed to Medium Crosswinds (Front View) 40

37 Time-Averaged Far-Field Fire Plume Velocity Magnitudes Exposed to Medium Crosswinds (Front View) 41

LIST OF TABLES

Table		Page
1	A Summary of Experimental Case Studies Employed for Computational Model Validation	8
2	A Summary of the Computational Modeling Approach Taken to Predict Aircraft Crash Pool Fire Events	9
3	A Summary of Experimental Case Studies Used for Computational Model Validation	10
4	A Summary of Aircraft Wetted Surface and PCA Ratios	28
5	A Summary of Aircraft Fuel Capacity and Passenger Limitations	28
6	A Summary of Time-Averaged Mean Aircraft Surface Thermal Signatures	32

LIST OF ACRONYMS

CFD	Computational fluid dynamic
CPU	Central processing unit
CSAFE	Center for the Simulation of Accidental Fires and Explosions
DAQ	Data acquisition
DO	Discrete ordinates
DOE	Department of Energy
DPG	Differential pressure gage
FAA	Federal Aviation Administration
FDS	Fire Dynamics Simulator
HFG	Heat flux gage
K	Kelvin
LES	Large-Eddy Simulation
NAWCWPNS	Naval Air Warfare Center Weapons Division
NFPA	National Fire Protection Association
NIST	National Institute of Standards and Technology
NLA	New Large Aircraft
PCA	Practical critical area
RACFM	Risk Assessment Compatible Fire Model
RANS	Reynolds-Averaged Navier-Stokes
Re	Reynolds number
SIMPLE	Semi-Implicit Method for Pressure-Linked Equations
SNL	Sandia National Laboratories
TC	Thermocouple
TI	Turbulence intensity

EXECUTIVE SUMMARY

New Large Aircraft (NLA) pose unique firefighting challenges not previously considered for traditional aircraft. Specifically, questions have arisen regarding the applicability of current firefighting protection standards to nonconventional design changes, such as fuselage shape modifications, enhanced material compositions, new fuel storage locations, and unique passenger loading configurations. To address fuselage shape concerns, a computational fluid dynamic (CFD) modeling strategy was developed to quantify heat transfer to the aircraft for a given aircraft geometry and hydrocarbon pool fire condition.

A brief review on large-scale pool fires and their interactions with engulfed bodies both from an experimental as well as computational perspective is initially presented. Experimental data published by the Fire Science and Technology Division of Sandia National Laboratories and the Naval Air Warfare Center Weapons Division on a large-scale mock fuselage engulfed in a hydrocarbon pool was used to validate the CFD methodology for low- to medium crosswind conditions; a range defined by combustion and turbulence modeling assumptions. The validated CFD process was then applied to two NLA geometries (Boeing 777 and Airbus A380) and one traditional platform (Boeing 707) to exercise the model's applicability using the National Fire Protection Association 403 standard practical critical area fire condition.

The CFD predictions supported experimental conclusions showing increased crosswinds amplify heat transfer to the aircraft surface due to enhanced turbulent fuel-air mixing. Based upon the predicted CFD fire plume structure and aircraft surface heat transfer magnitudes, nominal changes in aircraft geometry exposed to similar scale flame and atmospheric conditions pose no extraordinary firefighting challenge.

1. INTRODUCTION.

1.1 BACKGROUND.

Due to the number of New Large Aircraft (NLA) operations established in several major U.S. airports, the Federal Aviation Administration (FAA) commissioned a review of current firefighting protection standards currently based upon traditional aircraft [1].

NLA are defined by their oversized dimensions; full-length, double-deck cabins; enhanced material composition; and unusual fuel storage locations. Figure 1 depicts the relative size of the NLA Airbus A380 compared to an older-generation Boeing 747 large-frame aircraft [2] and via an internal schematic that highlights the locations of advanced composites [3].

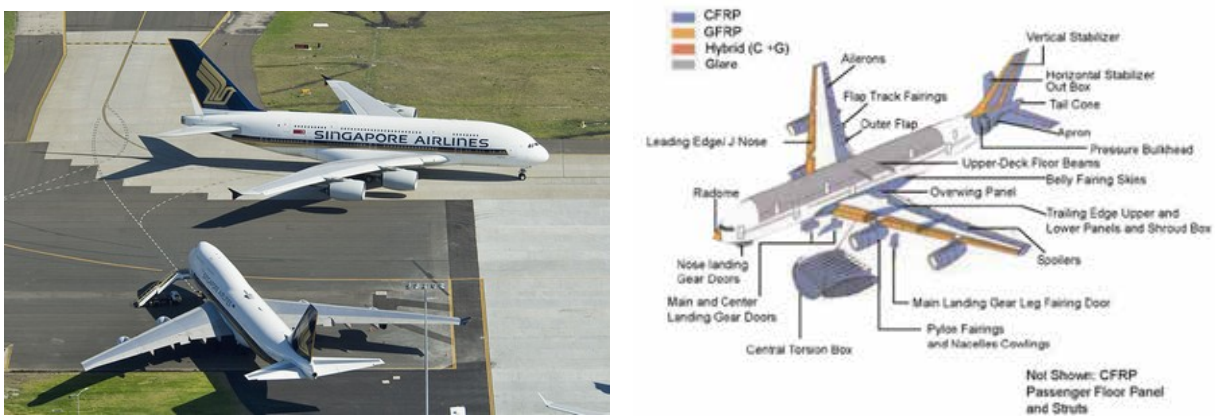

(a) (b)

Figure 1. The NLA A380 in (a) Relative Size Comparison to the B-747-400 (pictured on the bottom) and (b) a Composite Profile Map of the A380

The FAA has supported multiple research efforts to investigate risk assessment metrics for aircraft post-crash fire environments. Programs have encompassed a variety of strategies including experimental, analytical, as well as computational modeling approaches [3-5]. More recently, the FAA supported construction of a partial full-scale NLA mockup at the Air Force Research Laboratory's fire research facility at Tyndall Air Force Base for conducting aircraft rescue firefighting research. Figure 2 illustrates a fully developed JP-8 liquid pool fire engulfing the NLA mockup and post-flame conditions from a different perspective, thermally quantified by infrared.

(a) (b)

Figure 2. The NLA Mockup (a) Engulfed in a JP-8 Pool Fire and (b) After the JP-8 Pool Fire Using Infrared Imagery

Although full-scale fire testing is critical to fire research, it has some disadvantages. Fuel costs can be prohibitive. Outdoor studies, which are necessary for NLA analysis due to the massive spatial scales involved, must contend with chaotic atmospheric influences that typically result in significant variance between repeated trials. Experimental setups also encounter data acquisition (DAQ) challenges regarding measurement certainty; and embedded instrumentation is often restricted to a few finite points, offering a limited scope of the flow field. In addition, the destructive combustion environment results in reduced life expectancy for both fabricated test and DAQ equipment.

1.2 SCOPE.

To supplement full-scale fire tests, a computational fluid dynamic (CFD) simulation strategy was developed. The objective of the CFD was to predict the major combustion plume flow features as well as thermal heat transfer magnitudes to aircraft bodies immersed in hydrocarbon pool fires that are consistent with an accidental post-crash fire event. The CFD offers an alternative approach for obtaining predictive estimates of fire scenarios too impractical or costly to evaluate experimentally.

This research consisted of a literature review, selection of the CFD software suite, and simulation development. The literature survey briefly introduces the physical principles associated with large-scale hydrocarbon liquid pool fires, their interaction with engulfed bodies, along with a brief overview of pool fire modeling.

An industry-accepted, commercially available CFD software suite entitled ANSYSâ FLUENT® was selected as the analysis tool to ensure continued physical model development and accessibility in the public domain. Its hybrid mesh capability also provides advantages involving complex geometries in which most exclusive fire modeling codes still face limitations. The methodology is initially presented and validated using experimental data published by Sandia National Laboratories (SNL) in conjunction with the Naval Air Warfare Center Weapons Division (NAWCWPNS), and then applied to particular aircraft of interest.

The primary objective of this research was to develop the CFD simulation. Special attention was paid to the role aircraft geometry plays in altering localized pool fire combustion flow dynamics, specifically fuselage shape, wing planform, and engine configuration. Using similar fire conditions, results were obtained comparing the time-averaged thermal response between different aircraft. Results were intended to provide supplemental risk assessment metrics to support firefighting protection needs for current and future generation aircraft. The long-term contribution of this work aims to support an integrated modeling simulation strategy accounting for aircraft post-crash dynamics, accidental fire scenarios, as well as fire suppression interaction to supplement auxiliary research initiatives.

2. LITERATURE REVIEW.

2.1 OVERVIEW.

Literature was compiled that examined the flow characteristics of large-scale hydrocarbon pool fires described experimentally as well as computationally, especially those involving interactions with immersed bodies. For this study, a large-scale pool fire is defined as a non-premixed, buoyant diffusion flame established over a two-dimensional (2-D) horizontal liquid, heavy hydrocarbon fuel surface. A heavy hydrocarbon is characterized by properties consistent with aviation jet fuels representing common diesel derivatives, such as Jet A and JP-8. Pool diameters are assumed to be much greater than 1 m to coincide with spatial scales associated with full-size commercial aircraft.

Due to the lack of computational power available to solve all-inclusive field models with accuracy and resolution, the majority of relevant information prior to the mid-1990s focused on experimental and observational data. The following summary focuses on three categories including the physical characteristics of large-scale pool fire dynamics, their interaction with engulfed bodies, and the computational developments taken to complement analytical and experimental efforts.

2.2 PHYSICAL CHARACTERISTICS OF LARGE-SCALE POOL FIRES.

Several reviews discussing hydrocarbon pool fire physics summarize most of the literature compiled over the past few decades [6-10], most recently by Steinhaus et al. [11], who focuses on large-scale pool fires resulting from accidental spills. Steinhaus separates the fire into five distinct zones including (1) the liquid fuel, (2) the unburned fuel vapor cone immediately above the liquid fuel, (3) a luminous combustion flame region surrounding the fuel vapor cone, (4) an intermittent turbulent combustion zone above the luminous flame, and (5) a nonreacting buoyant plume shrouding the interior zones [11]. These zones are described as being physically interdependent by nature requiring mathematical closure to provide quantitative definition to each. Together, the system harbors complexities associated with a multiscale, multiphase, chemically reacting turbulent environment [12]. Steinhaus recaps metrics critical to characterizing the flow through each zone: fuel burn rate (or mass loss rate), heat release rate (or the total energy released from the fire), flame height (loosely defined as distance from the fire base to the flame tip with at least 50% intermittency), smoke production rate, and radiation released (or emissive power). These factors are driven by a variety of elements ranging in sophistication. A few common descriptors include pool geometry, fuel composition, ventilation

conditions, adjacent geometry, and bounding substrate [11]. Experimental methods quantifying these characteristics are uniquely discussed by several researchers employing various techniques [13-23].

It is speculated that the principal vortical flow structures that uniquely identify large-scale pool fires similar to that shown in figure 2 are the result of baroclinic, or stratification of vortex pairs produced from the buoyant collision of sequentially smaller flow structures [12]. Generated by the turbulent energy cascade, pool fires contain a wide range of temporal and spatial scales within these structures responsible for various characteristics. Larger turbulent scales at relatively low frequencies (often described as an intermittent pulsation, or vortical eddy shedding) shape overall plume dynamics, which drives global air ingestion levels and low-order interaction between the combustion plume and surrounding air. Conversely, finer, high-frequency turbulent flow scales directly control local fuel-air mixing and combustion rates [10]. Visible pulsation frequencies dominated by large-scale structures are well described and are found to decrease with pool fire diameter through simple empirical correlations using Froude and Strouhal dimensionless numbers. These transient pulsations are also believed to be highly reliant upon soot production [12].

Large-scale pool fire heat transfer is dominated by radiation where the fuel burn or recession rate becomes nearly independent of increasing pool diameter. This is due to saturated soot levels creating an optically thick environment resulting in strong radiation feedback to the liquid fuel-vapor surface. In opposition, small-scale (<2 m) pool fires are dominated by convection heat transfer where soot production is sustained at lower levels. Ventilation or wind effects can also greatly influence large-scale dynamics through enhanced mixing in the combustion region, which causes increased chemical reaction rates and elevated flame temperatures. In addition, high crosswind environments skew radiation profiles that can significantly change fuel vaporization levels, which further complicates the heat transfer process. Pool bounding structures can also alter pool fire dynamics by modifying thermal resistance. Soot production remains a challenging but important subject matter as its production and transport is heavily reliant upon high-order, nonlinear interacting turbulence, temperature, and fuel composition effects [12]. Although various studies have characterized different physical aspects of soot, it remains a focal point of ongoing research [24-26].

2.3 OBJECTS IMMERSED IN LARGE-SCALE POOL FIRES.

Pool fire physics are further complicated by the introduction of engulfed objects to the flame front. These object-thermal interactions increase in significance as the ratio of object size to fire size increases. The majority of experimental work conducted on objects engulfed in large-scale hydrocarbon pool fires stems from joint investigations lead by SNL and NAWCWPNS. Research sponsored by the U.S. Department of Energy (DOE), the Nuclear Regulatory Commission, and the Department of Transportation examined the effect hydrocarbon pool fire dynamics on engulfed mockup structures simulating the aircraft post-crash fire environment. Similar studies pertained to shipping containers of hazardous materials in similar combustion

environments [27 and 28]. Objectives from these studies summarized by Koski et al. are listed below.

- Enhance the understanding of fire phenomenology.
- Estimate empirical parameters for Risk Assessment Compatible Fire Models (RACFMs).
- Provide validation assistance for fire models.
- Expand the thermal response database of objects engulfed in pool fires [29].

Early experiments conducted on a water-cooled (constant surface temperature) calorimeter helped determine radiation absorption coefficients and demonstrated that gray gas models provide a reasonable description in a soot-laden environment [29]. The first in a series of mock fuselage tests involving large steel cylinders engulfed in jet fuel fires quantified the effects of turbulent combustion environments exposed to various conditions. Results showed a rise in flame temperature and surface heat flux accompany turbulent recirculation zones subject to accelerated fuel-air mixing. These elevated zones were found on the leeward edge, or wake region of the immersed object with gains proportional to the crosswind strength [30]. Subsequent SNL testing analyzing object-thermal response relative to pool fire diameter can be found in associated reports [31-33]. These reports focus on instrumentation development and error quantification. Data from the test series published by Gritzo and Suo-Antilla [33] was extracted to provide validation data for the CFD modeling approach employed for this study.

2.4 LARGE-SCALE POOL FIRE MODELING.

The majority of relevant experimental work supports the verification and validation of computational fire models to aid in probabilistic risk assessment. In the mid-1990s, the FAA commissioned SNL via an interagency agreement to analyze the technical issues involved with fire modeling, as well as to plan research steps to address future requirements. Fire models were broken down into four major categories [5].

- Zone models that are largely based upon correlated experimental data that was tuned for specific regimes typically providing rapid solutions for compartmental or enclosure fires.
- Field models (the application of this effort) focused on first principle, physical interactions that generally require intensive computing power, are more robust than zonal models, and are less restrictive on geometry driven scenarios of interest.
- Pyrolysis, or material burning models, that require closed-loop feedback between gaseous combustion and solid devolatilization/breakdown.
- RACFM derived from a combination of the above models that was optimized to solve the dominant physical processes driving combustion and heat transfer [5].

SNL concluded that field models offered the most reliable approach for fire modeling, noting further work in turbulence modeling, soot generation, and radiation properties of soot-laden gases was needed. Model sensitivity analyses and experimental validation data were highlighted as key contributors to an overall proposed research plan. Two SNL fire research codes analyzed, VULCAN and the SNL Gray Gas Model, provided agreeable results compared to available

experimental data. In general, it was found that computational fire-modeling tools provided valuable qualitative and quantitative analysis of aircraft-fire-related problems [5].

Because hydrocarbon pool fire dynamics are dominated by a wide range of length and time scales, high-fidelity resolution of these interacting scales pose the greatest challenge. Because they are computationally efficient, physical modeling approaches resolve the dominant physical transport process typically defined by a finite, narrow range of scales. The wider the spectrum, the more computationally intensive the solution process becomes. A review of all the interacting fluid and combusting temporal and spatial scales can be found in a summary by Tieszen [34]. A detailed overview of several industry-accepted fire field submodels and their advantages and disadvantages can be found in a text by Yeoh and Yuen [35]. A short survey of supplemental work investigating various numerical approaches to solving different aspects of the general hydrocarbon pool fire problem is also highlighted [36-40]. The physical submodels implemented for this study are briefly discussed in section 3.3.

Fire Dynamics Simulator (FDS), a popular field-modeling approach available through the National Institute of Standards and Technology (NIST), is a CFD solver specifically formulated for low-speed, thermally driven flows characteristic of accidental fires. Although it is considered a research code, several add-on packages tailored for flow visualization and user-friendly post-processing make FDS an attractive computational engineering tool for fire modeling. For the most part, the developmental history of FDS focused on internal fire scenarios; however continued development has extended applicability to external hydrocarbon-fueled environments. Mathematical model details and user implementation can be found at the official NIST website [41]. FDS currently relies strictly on rectilinear coordinates, or the enforcement of structured grid topologies in the geometric domain. Because high-fidelity resolution of the complex curvature of commercial aircraft geometries required unstructured mesh entities for this particular study, FDS was not considered.

More recent research by the Center for the Simulation of Accidental Fires and Explosions (CSAFE), a DOE Advanced Simulation and Computing Center, has further advanced understanding of large-scale pool fire dynamics through the development of a unique, sophisticated in-house simulation framework in conjunction with dedicated computational resources. Their work, similar to SNL, centers on risk assessment of objects immersed in pool fires from the perspective of weapons safety. Although the program was decommissioned in November 2010, uncertainty quantification, radiation modeling in complex fire simulations, and advanced, detailed chemistry methods for soot generation and deposition are among the many critical subfields still actively investigated. A complete list of associated CSAFE publications can be found at the official CSAFE website [42], in addition to synopsis papers summarizing past work [43-45].

3. COMPUTATIONAL MODEL VALIDATION.

3.1 OVERVIEW.

Validation case studies were selected based upon well-established test procedures, clarity of overall design and boundedness, as well as depth of measurement detail. Geometric simplicity was also a contributing factor to reduce errors prone to complex meshing environments. CFD

models were constructed to reflect the experimental spatial domain and appropriate boundary conditions to compare results. A test sequence reported by the Fire Science and Technology Division SNL in coordination with the NAWCWPNS was selected. The test series was established to support Weapons System Safety Assessments in the scenario of transport aircraft exposed to a large fuel fire. Its main focus was the study of heat transfer effects of a cylindrical fuselage shape reminiscent of a military transport aircraft partially engulfed in a hydrocarbon pool fire. Test objectives mandated the data be presented in a context suitable for comparison to computational model predictions. Its purpose was intended to spur further development of fire models that could be used to address other complex fire scenarios of interest. In addition, the study was part of a minority of experiments that detail thermal response at similar physical scales to that of commercial passenger aircraft where engulfed body and flame dynamics are strongly interdependent [33].

3.2 EXPERIMENTAL SUMMARY.

Computational validation models were defined to reflect setup and operating conditions from experimental trials conducted at the NAWCWPNS CT-4 test site. Test geometry consisted of a corrugated 3.66-m diameter, 18.28m-long culvert welded shut at both ends and supported 0.6 m above the leeward edge of an 18.9-m diameter JP-8 jet fuel pit. The test pit was 25-cm deep, about 10 cm of JP-8 floating atop approximately 15 cm of water. Ignition was prompted at 3 locations via a 110 V electrical signal. Testing concluded once all the fuel was burned. The cylindrical culvert was made of 16-gage (0.16-cm-thick) carbon steel wrapped internally with approximately 5 cm of ceramic fiber blanket insulation to protect instrumentation and prolong structural life. An array of heat flux gages (HFGs) and thermocouples (TCs) measuring total heat flux and temperature, respectively, were arranged around the surface of the cylinder, beneath and along the liquid fuel surface, and in suspended vertical locations above the liquid fuel surface. The cylinder surface was characterized in three locations equally spaced 3.66 m about the culvert centerline identified as the central (C), western (W), and eastern (E) location. Similar instrumentation was also placed just outside of the flame zone to compare relative effects. Differential pressure gages (DPGs) were installed lengthwise on the culvert surface on the windward and leeward sides parallel to the prevailing wind direction at the central, western, and eastern locations. A final set of DPGs was stationed on the fuel pool surface and outside of the flame zone to monitor pressure gradients generated by the combustion process relative to the far field. Free stream, time-accurate wind speed and direction were recorded using vane-type gages positioned far enough away from the fire plume to minimize exposure to air entrainment induced by the fire plume [33]. Figure 3 depicts the actual experimental setup with an aerial schematic view highlighting the approximate locations of HFG, TC, and DPG.

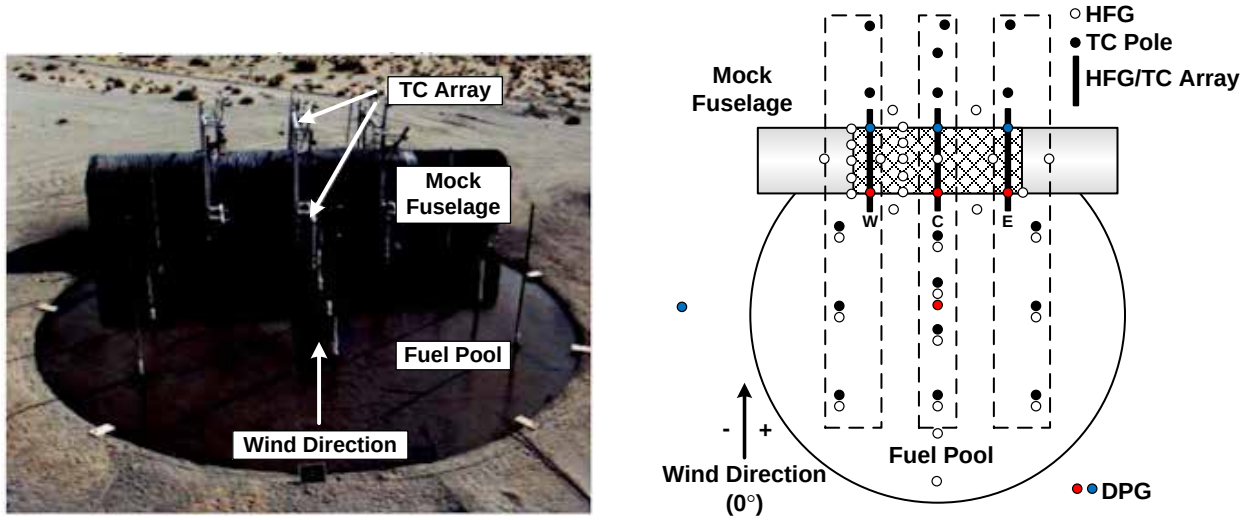

(a) (b)

Figure 3. The Experimental Set-up Showing (a) the C-141 Mock Fuselage in a 20-m-Diameter Fuel Pit and (b) an Overhead Schematic With Approximate DPG, HFG, and TC Locations (Adapted from reference 33.)

During the DAQ process, periods of quasi-steady state crosswind and fire plume behavior were recorded. Three experiments out of a possible eight reported were identified for comparison to CFD model results covering what will be referred to as a low (1.9 $m \cdot s^{-1}$), medium (5.4 $m \cdot s^{-1}$), and high (10.2 $m \cdot s^{-1}$) mean velocity crosswind condition. These cases were selected because they had the lowest root mean square (RMS) velocity magnitude fluctuations, or most consistent wind speed and direction out of the available trials. Table 1 summarizes the three experimental cases selected for comparison to CFD results. Time after ignition denotes the quasi-steady time period where DAQ took place. Wind velocity and direction are described by an average magnitude and its associated standard deviation.

Table 1. A Summary of Experimental Case Studies Employed for Computational Model Validation [33]

CaseName	Time AfterIgnition (s)	Wind VelocityMagnitude ($m \times s^{-1}$)	Wind Direction (°)
Low	225-350	1.9 ±0.2	-36.9 ±5.7°
Medium	400-575	5.4 ±1.2	11.4 ±12.5°
High	300-600	10.2 ±1.7	-22.7 ±8.3°

An average fuel recession rate of 4.4 $mm \times min^{-1}$ within the fuel pit was derived from the unsteady temperature change recorded by TCs located along vertical arrays positioned through the water, fuel, and flame zone. A fuel consumption rate of 0.058 $kg \times m^{-2} \times s^{-1}$ was extrapolated based upon fuel pool geometry and physical properties associated with JP-8. An average fuel surface temperature of 508 K was recorded for all trials. Figure 4 shows instantaneous screen captures

of a fully developed fuel fire engulfing the mock fuselage at the medium crosswind condition and the medium crosswind time-averaged over the quasi-steady period [33].

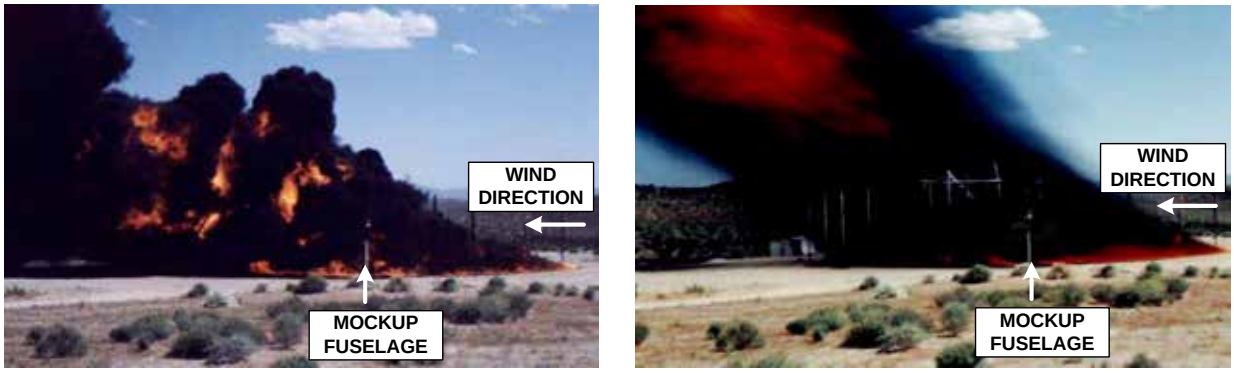

(a) (b)

Figure 4. Adapted Instantaneous Screen Capture of the Mock Fuselage (a) Fully Engulfed in Fire Exposed to a Medium Wind Condition and (b) a Time-Averaged Video of the Same Conditions (Adapted from reference 33.)

3.3 COMPUTATIONAL MODEL SETUP.

It is well established that multiscale turbulent flow mixing, interacting chemical kinetic combustion processes, radiation heat transfer effects, and soot production are the main features that drive large-scale accidental fire plume dynamics [11 and 12]. Multiple physical submodels were solved simultaneously using ANSYS® FLUENTâ to approximate this complex phenomenology. Through trial and error of mechanisms with varying degrees of fidelity, a solution framework was created to accurately and practically predict the experimental validation conditions. The software's compatibility within a multiphysics environment and support for complex mesh topologies reinforced its choice over alternatives. Table 2 summarizes the computational methodology implemented with each physical submodel, which are summarized in subsequent sections. The approach is applied to simulate the fire environments measured in the experimental validation study presented in section 3.2. Geometric mesh and boundary condition details conclude the summary.

Table 2. A Summary of the Computational Modeling Approach Taken to Predict Aircraft Crash Pool Fire Events

Physical Submodel	Physical Submodel Description
3-D Navier Stokes	Conservation equations of fluid motion
Non-premixed combustion	Chemical reaction kinetics
Realizable *k*-e	Turbulence
Discrete ordinates (DO)	Radiation heat transfer
Moss-Brookes	Soot production

3.3.1 Turbulence.

Large-diameter (>1 m) hydrocarbon pool fires are characterized by their periodically oscillating but intrinsically chaotic thermally buoyant plume. These physical traits are indicative of a fully turbulent flow structure. Turbulent flow quality is defined by the Reynolds number (Re), which describes the ratio of inertial to viscous forces in a particular system; the higher the Re, the more turbulent the flow quality. Another metric examines the turbulence intensity (TI) contained within the flow, or ratio of magnitudes between the fluctuating and mean flow components. Table 3 outlines the TI and the Re associated with each validation case. Because Re designation relies on a characteristic length, two values were calculated—one based upon the fuel pit diameter (18.9 m), and another based upon the mock fuselage diameter (3.66 m). Transition to turbulent flow over a 2-D cylinder (i.e., mock fuselage) begins around a Re of 10^5 [46]. With the lowest calculated value from table 3 on the order of 10^5, the flow domain was assumed fully turbulent.

Table 3. A Summary of Experimental Case Studies Used for Computational Model Validation (Adapted from reference 33.)

Case Name	Wind Velocity Magnitude ($m \times s^{-1}$)	Turbulence Intensity (%)	Reynolds Number (Re)	
			$Re_{Cylinder}$	Re_{Pool}
Low	1.9	10.5	4.76×10^5	2.45×10^6
Medium	5.4	22.2	1.35×10^6	6.99×10^6
High	10.2	16.7	2.56×10^6	1.32×10^7

The addition of turbulence equations was an unfortunate but necessary requirement because not all of the spatial and temporal scales associated with the high Re hydrocarbon pool fire flow environment can be explicitly modeled. The time-averaged Reynolds-Averaged Navier-Stokes (RANS) equations simulated turbulent flow conditions via the realizable k-ϵ model [47]. This method proved most effective in capturing the experimentally observed near-field mean flow structures and overall heat transfer to immersed structures while still maintaining robust numerical stability. Turbulence equations require auxiliary turbulent boundary conditions. Proper boundary conditions were often not obvious, and generally have a strong effect on computational stability. Turbulent kinetic energy (k) and eddy dissipation rate (ϵ) boundary conditions were derived from the TI of the flow and large-scale eddy (characteristic turbulent) length. The TI was extracted from table 3 wind velocities for each case. The turbulent characteristic length was more ambiguous, frequently generalized by a relationship with the characteristic length and the overall flow domain. An expression correlating the local boundary layer thickness to the large-scale eddy length produces a value of 0.256 m, which was used for each validation case [48].

3.3.2 Combustion.

Chemical reaction kinetics were simulated using the non-premixed combustion model in which heated jet fuel vapor was injected at the location of the horizontal liquid pool surface normal to the oncoming turbulent atmospheric cross flow. As the fuel vapor mixed with the entraining

oxygen, a fast chemistry or "mixed-is-burnt" approximation was used to determine the resulting combustion plume characteristics. Also referred to as the mixture fraction approach, this method employed a probability density function to statistically determine the local combustion chemistry and thermodynamics based upon local fuel-air turbulent mixing. This approach was valid for most of the flow field since chemical reaction time scales are much faster compared to turbulent fluid motion time scales present in pool fire combustion plumes. These assumptions can lose validity as crosswinds amplify formulating quasi-premixed conditions before combustion initiates. Figure 5 relates the chemical and physical flow time scales graphically. Because the large spatial scales of a full-scale aircraft fire environment demand significant computing resources, the non-premixed combustion was further advantageous requiring the solution of only two more transport equations: the mixture fraction mean and variance [35].

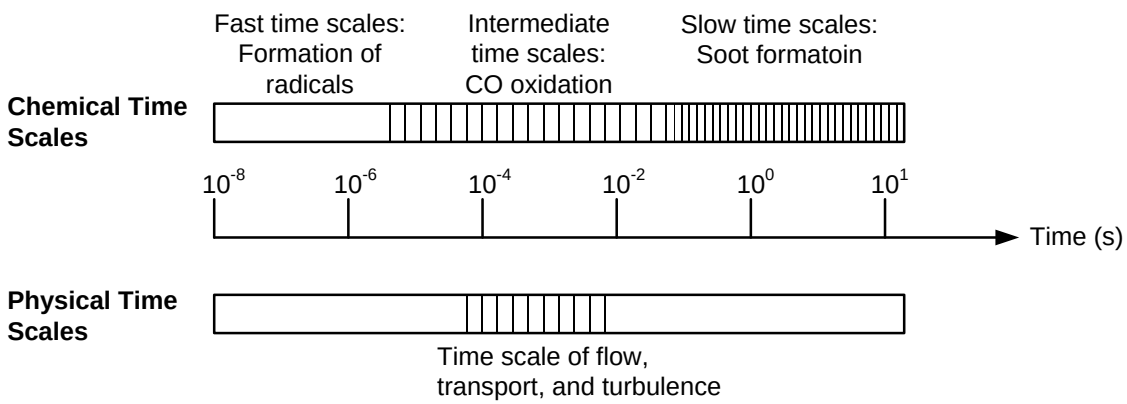

Figure 5. Comparison of Physical and Chemical Combustion Time-Scales
(Adapted from reference 35.)

Energy terms were treated non-adiabatically to allow for heat transfer to the surrounding flow field and engulfed structures. Inlet diffusion was activated to allow for enhanced fuel air mixing near the pool surface as evidenced by the experimental observations. Because the standard FLUENT Jet A chemical mechanism was chemically analogous to JP-8 for the purpose of this study, it was implemented for the fuel [48].

3.3.3 Radiation Heat Transfer.

For significantly large-diameter hydrocarbon pool fires, radiation heat transfer plays a critical role in overall heat transfer due to the emissive power of the flame zone participating with the local surroundings. Heavy hydrocarbon mixtures, such as JP-8 and other diesel derivatives, typically do not burn stoichiometrically in ambient air due to naturally occurring oxygen-rich and oxygen-starved currents induced by the thermally buoyant plume. This causes inefficient combustion and in turn produces heavy soot, which absorbs a large portion of the emitted radiation, as evidenced in figure 2(a). Radiation heat transfer was described by the discrete ordinates (DO) model. The DO model solved the radiation heat transfer equation in a transport (non-ray tracing) format analogous to the energy and fluid flow equations of motion. Radiation intensity was solved for using a preset number of discrete solid angles projected through the flow domain from the radiant source through the participating medium—in this case, the air and combustion-related species and products. Gray gas model assumptions were applied to

approximate jet fuel fire conditions as radiant intensity does not vary significantly with wavelength [48 and 49].

3.3.4 Soot Formation.

Soot formation plays an integral role in determining the amount of local energy absorbed during the combustion process and in turn affecting the total heat transfer to objects engulfed in the flame zone. Soot generation was governed by the Moss-Brookes method, which solves soot nucleation and growth as a general transport function analogous to the conservation equations. The Moss-Brookes method provided the most accurate heat absorption balance to generation sources and was the best method to match experimental validation flame temperatures. It also provided a more qualitatively accurate particulate cloud compared to other approaches [50].

3.3.5 Physical Flow Domain.

The physical flow domain was designed to reflect the experimental validation conditions developed by SNL and NAWCWPNS. To minimize cell count, a multiblock hybrid mesh topology was generated using Pointwise Gridgen$^{\hat{a}}$. To accommodate multiple crosswind flow directions and minimize grid regeneration, a cylindrical far-field domain was used that allowed for rotational symmetry about a central vertical axis. A hexahedral, structured far field with high aspect ratio cells near the ground was used to resolve turbulent boundary layer effects. A structured topology also was used for the fuel pool and mock fuselage near field boundary zones. An unstructured block made of isotropic tetrahedrons and pyramids was used to link near field and far-field structured zones. Approximately 1.7 million cells were used for each case. Figure 6 shows a near-field schematic with relevant dimensions reflecting experimental schematics, and shows the near-field surface mesh of the mock fuselage, fuel pool, and local surrounding area. Figure 7 shows the geometric mesh in its entirety depicting the far-field, outer-cylindrical domain along with multiple interior cuts describing local grid topology.

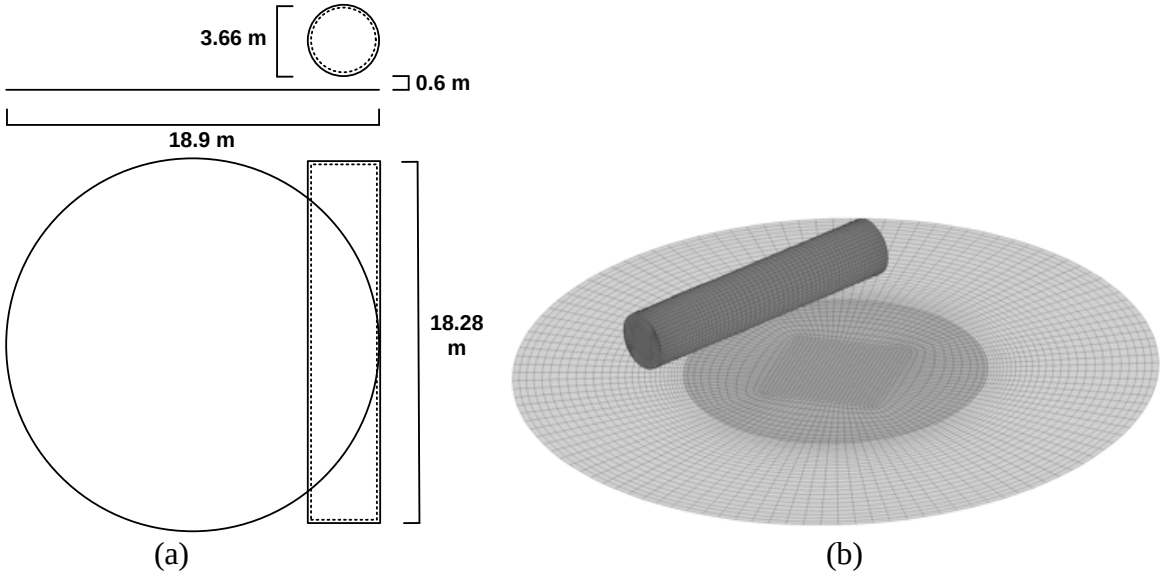

Figure 6. Experimental Validation Case Showing (a) a Near-Field View of the Relative Dimensions of the Fuel Pool and Mock Fuselage and (b) an Isometric View of the Equivalent Geometric Surface Mesh

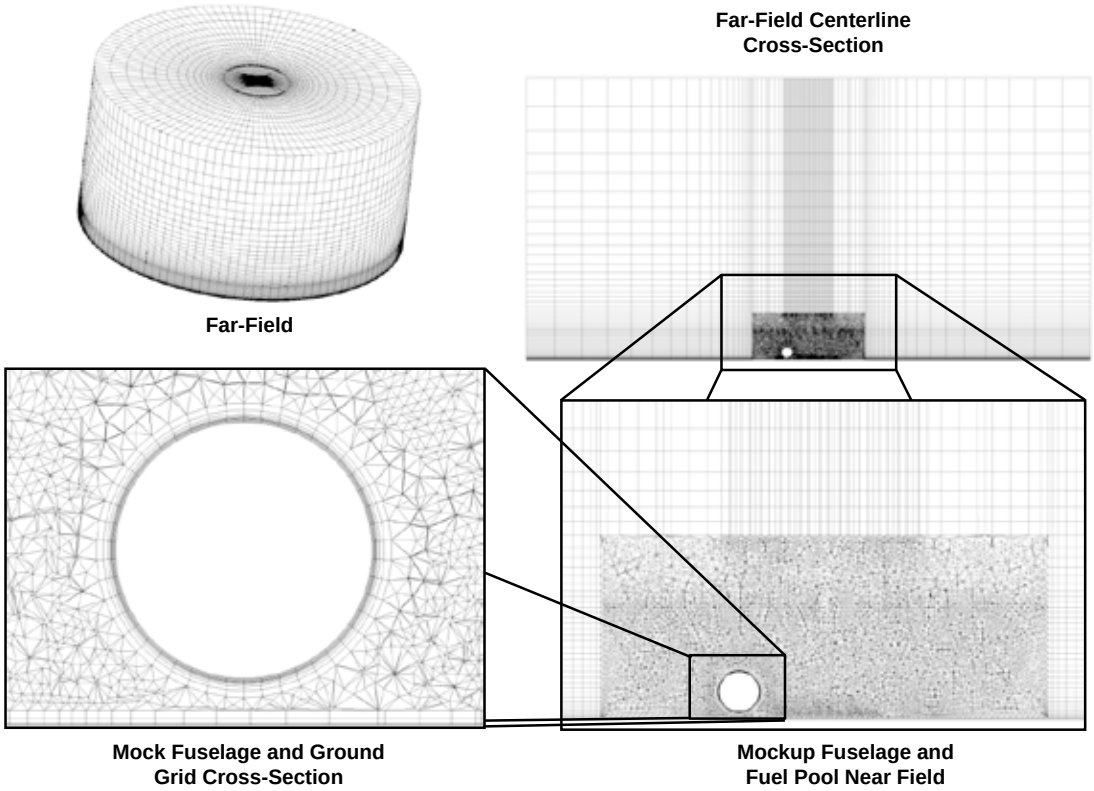

Figure 7. Experimental Validation Case Geometric Mesh

3.3.6 Boundary Conditions.

Boundary and operating conditions reflected the measurements recorded during the experimental validation where applicable, with some adjustments made for simplicity. To define the prevailing wind speed and direction, the cylindrical far-field boundary was divided into three surfaces. The windward far-field boundary was defined as a constant velocity inlet using the mean measured wind speed. The opposing leeward far-field boundary and the ceiling were defined as a pressure outlet to balance the flow. The fuel pool surface was treated as a gaseous mass flow inlet set at the mean temperature of 508 K recorded by experiments [33]. Fuel vapor was injected normal to the domain at 16.46 $kg \times s^{-1}$, a value extrapolated from the average fuel recession rate and pool geometry. The mock fuselage and surrounding ground area were modeled as infinitely thin, nonadiabatic walls. All bounded surfaces besides the fuel pool fire inlet were initialized to 300 K to simulate start-up conditions. As steady-state combustion conditions equilibrated during the solution process, convective and radiation heat transfer forced the mock fuselage, the flame zone, and the surrounding ground area to heat up. Fuel pool mass flow inlet conditions also floated to accommodate feedback from the flow domain, although steady-state conditions stayed very close to the prescribed conditions. Figure 8 shows the location and boundary conditions enforced relative to the far field. Figure 9 depicts boundary conditions from the near field perspective.

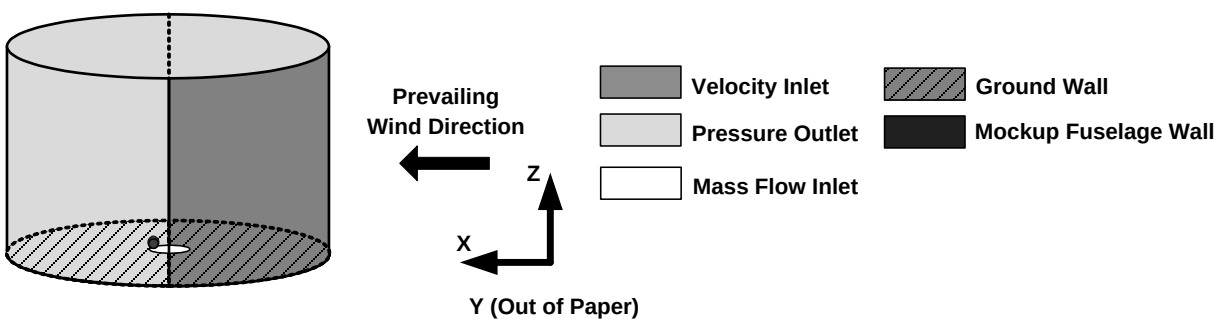

Figure 8. Far-Field Schematic Outlining CFD Boundary Types and Conditions

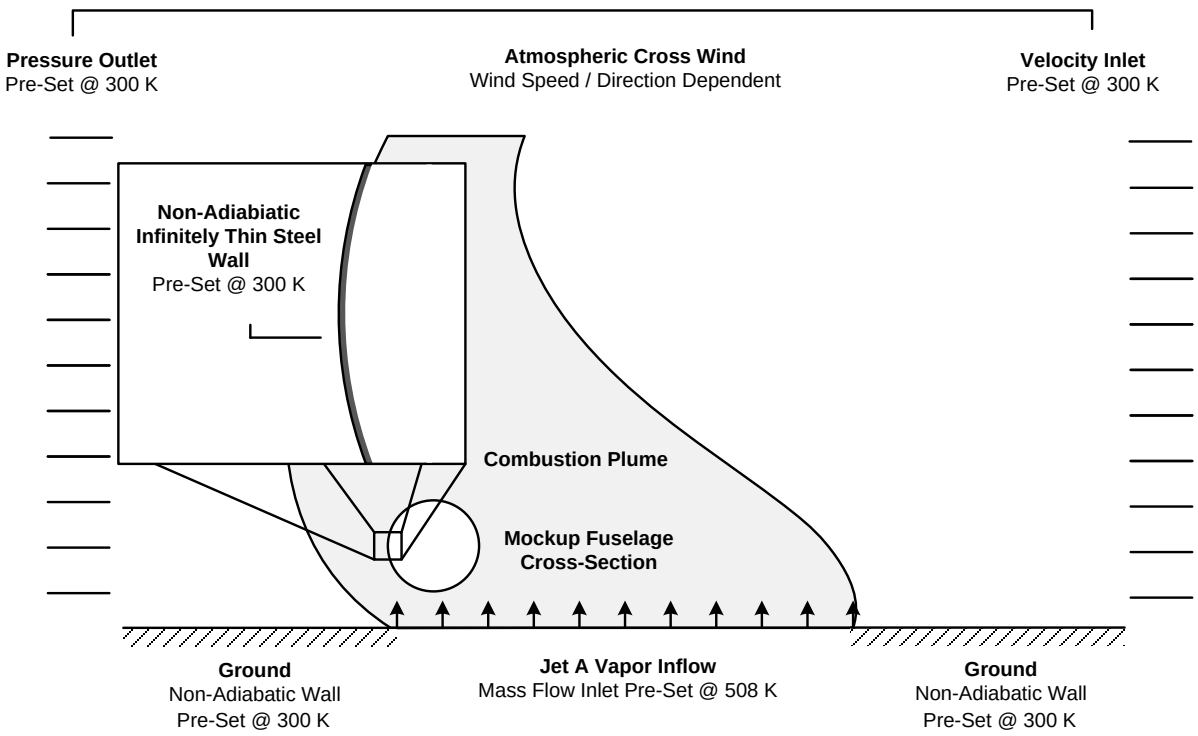

Figure 9. Near-Field Schematic Outlining CFD Boundary Types and Conditions

3.3.7 Numerics.

Model simulations were executed using an implicit, segregated pressure-based solver using the SIMPLE (Semi-Implicit Method for Pressure-Linked Equations) algorithm for pressure-velocity coupling [48]. Steady-state simulations were solved with second-order spatial accuracy, with time-accurate solutions requiring first-order accuracy enabled for radiation transport to maintain solution stability. Temporal discretization was maintained using the bounded second-order implicit method. Time-accurate calculations were solved with a fixed time step. Although absolute convergence criteria were not enforced, residuals were observed to be on the order of 10^{-4} or lower.

3.4 RESULTS.

Computational validation cases were executed on an 8-processor Harpertown Intel® Xeon® workstation taking approximately 50 central processing unit (CPU) hours per case, or about 6 hours real time. All reproduced experimental data used for comparison was time-averaged over a finite time period as outlined in table 1. CFD model validation studies were solved steady-state. Mock fuselage surface pressure, heat flux, temperature, and flame temperature were the data sets compared.

3.4.1 Surface Pressures.

DPGs were installed on the mock fuselage surface to record the change in pressure between the windward stagnation surface and leeward trailing surface. Measurements were only available for

the medium wind condition case [33]. Figure 10 shows the unsteady experimental (EXP) DPG measurements for the mock fuselage (MF) west, center, and east locations, as well as the relative fuel pool (Flame) surface to far-field DPG described in section 3.2. The specific quasi-steady time period considered for data was recorded between the 6 min 40 s and 9 min 36 s mark. Figure 11 shows the equivalent CFD static pressure calculations for the west, center, and east locations reported at each discrete computational cell surface location around the mock fuselage circumference. The windward and leeward locations in addition to the fuselage top and bottom are highlighted with a black circle. Their locations relative to the mock fuselage circular cross-section is shown in the figure's lower-left corner. An average CFD differential pressure of about 55 Pa was reported for all 3 fuselage surface locations showing good agreement with the observed results. The CFD model calculated an approximate 12 Pa differential pressure for the flame, which also compared well to the experiment from figure 10. Figures 12 and 13 show the CFD total pressure and velocity vectors, respectively, in the mock fuselage near field along a centerline cross-section. The mock fuselage wake was asymmetric due to a combination of its proximity to the ground coupled with the thermal buoyancy generated near the fuel surface. Velocity vectors show a similar trend with corresponding local flow directions depicting the wake region characteristic of bluff-body shedding.

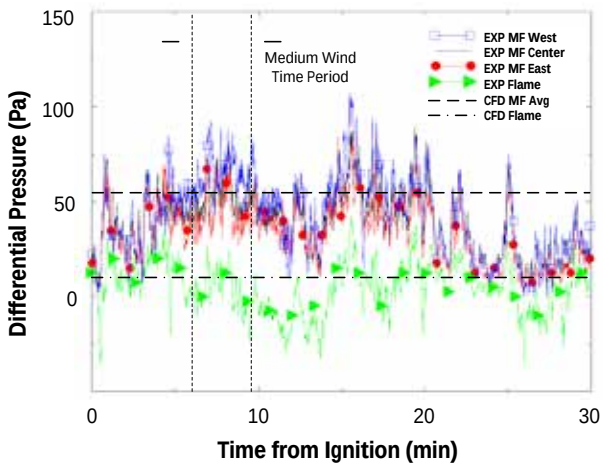

CFD = Computational Fluid Dynamic
EXP = Experimental
MF = Mock Fuselage

Figure 10. Medium Wind Condition Transient Experimental DPG Measurements on the Mock Fuselage Compared to Time-Averaged Steady CFD Results (Adapted from reference 33.)

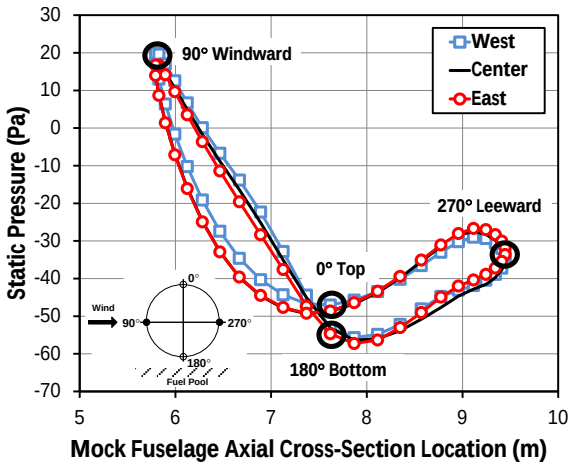

Figure 11. The CFD Static Pressure Calculated About the Mock Fuselage Cylinder

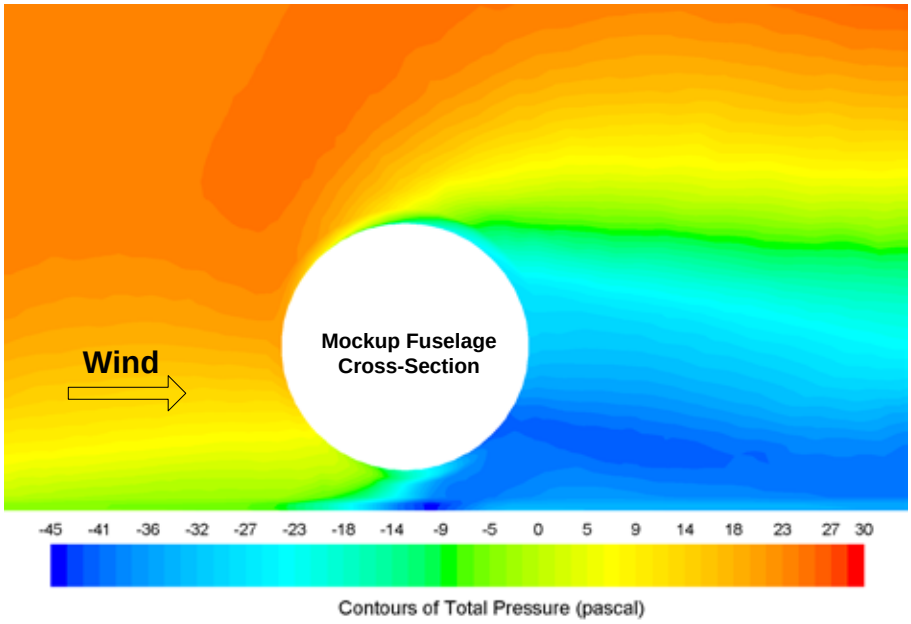

Figure 12. Centerline CFD Mock Fuselage Near-Field Total Pressure Contours of the Medium Wind Condition

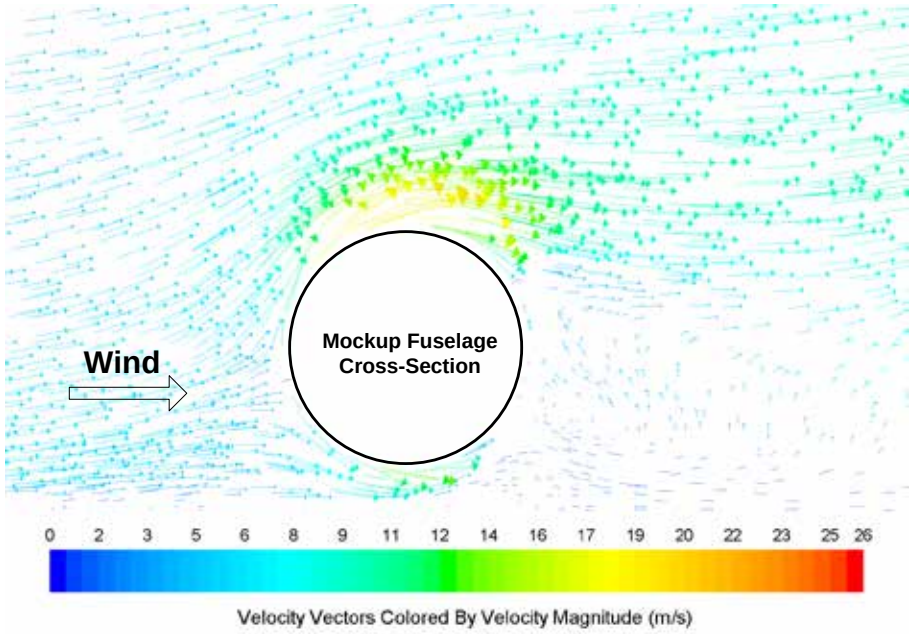

Figure 13. The CFD Mock Fuselage Near-Field Velocity Magnitude Vectors of the Medium Wind Condition

3.4.2 Flame Temperatures.

Experimental flame temperature measurements from the case studies outlined in table 3 were recorded and time-averaged using contour plots in three equally spaced planes perpendicular to the fuel pool in figures 14, 15, and 16. Experimental validation plots are aligned on the left, and the corresponding CFD plots are aligned on the right. Figure legends denoting each data plane are located to the far left on each plot. (See the dashed outlined planes from figure 3(b) for the detailed plane reference.) Plane measurements were approximated because all the TCs did not lie in the same exact plane. The intersection with the mock fuselage is represented by the black circular cross-section in each plot. Measured and calculated temperatures ranged from 300 K (ambient) to upwards of 1600 K within and near the flame zone. CFD color maps were converted to gray scale and discretized to reflect the same ranges reported experimentally [33].

Computational results compared well capturing similar magnitudes and profile trends. Similar agreement was illustrated for the low crosswind case, with the high crosswind case showing the greatest divergence most prevalent along the leeward side of the fuselage and adjacent trailing wake zone. Heat transfer was under predicted significantly in this regime. Because fuselage surface differential pressure data was unavailable for the high crosswind condition, it was difficult to speculate how the model broke down. From inspection, it was theorized turbulent flow separation was predicted prematurely creating a lifted flame condition and in turn minimizing the heat transfer to the leeward surface.

Figure 14 shows good agreement between experimental and CFD results for the low crosswind case. The low crosswind case maintained the most acute angle with respect to the mock fuselage position and depicted the greatest asymmetry in flow between each plane. The low crosswind

case also provided the lowest TI, or lowest ratio of wind fluctuations relative to the mean flow creating the calmest experimental wind condition. Still air to low crosswind conditions create the best conditions for a diffusion-dominated flame, reflecting an environment most suitable for the mixture fraction combustion approach taken. Figure 15 shows similar agreement for the medium wind case. The medium wind case had the most relative normal angle with respect to the mock fuselage position, which created the strongest symmetry among all cross-sections. This is visibly evident from the plots. Medium crosswind conditions generated the largest crosswind TIs of all three cases and provided the strongest flow mixing, which created the most favorable model conditions for RANS calculations. Figure 16 shows comparisons between the high crosswind cases showing significant disparity in leeward wake region flame temperature magnitudes. Here, two theories are postulated based upon employed model assumptions. Convective forces due to enhanced crosswind conditions created greater flow separation around the leeward side of the cylinder. With the employment of a simplified RANS turbulence model, flow separation, detachment, and downstream recirculation became increasingly hard to predict. Since recirculation enhances fuel-air mixing and elevates heat transfer, poor flow prediction in this area could affect thermal predictions. Further, higher crosswind forces challenge the assumptions made by the mixture fraction combustion modeling approach conducive to diffusion flames. With an increase in forced air entrainment, heated fuel vapors have a longer residence time to premix with a stronger prevailing wind before combusting. This can delay ignition sweeping high heat release zones away from highly turbulent fuel-air mixing zones.

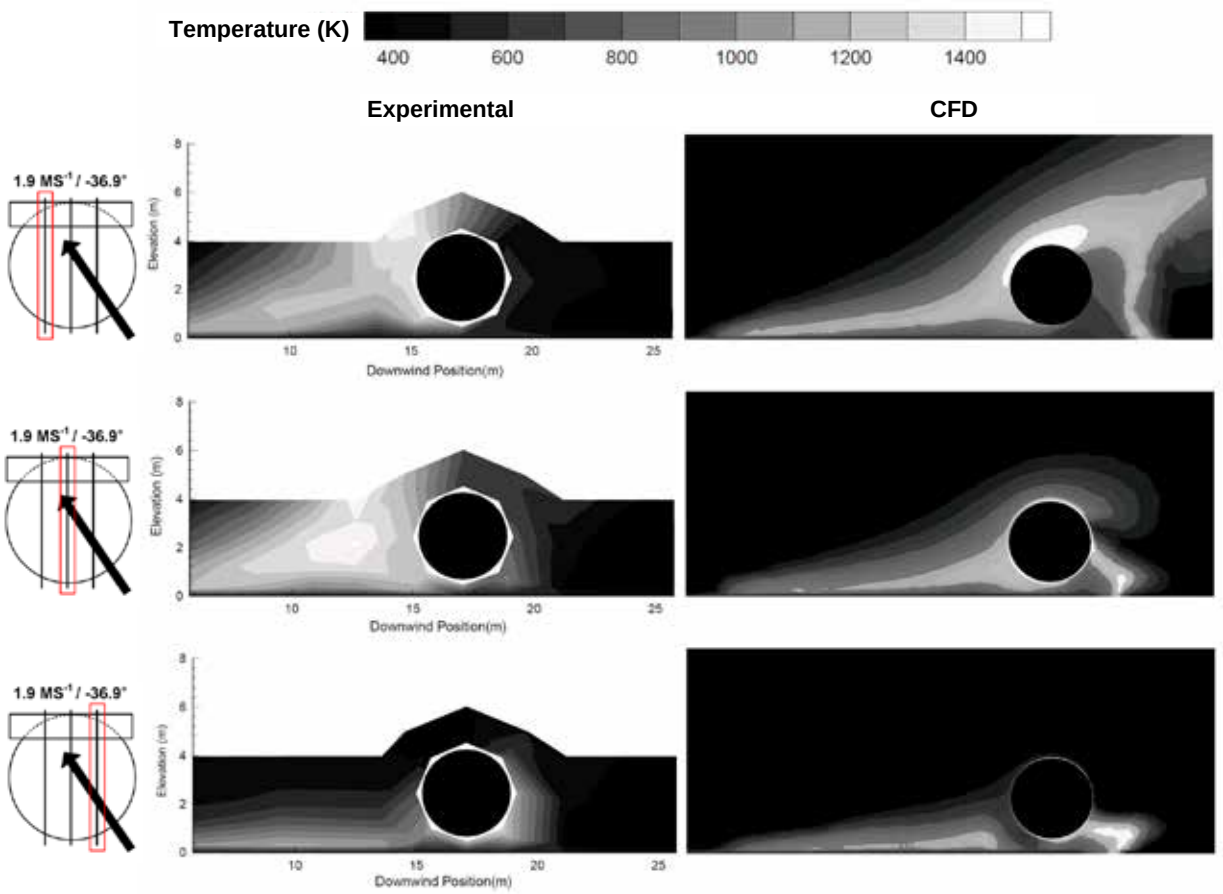

Figure 14. Low Crosswind Case Showing Flame Temperature Contour Comparisons (Experimental data was adapted from reference 33.)

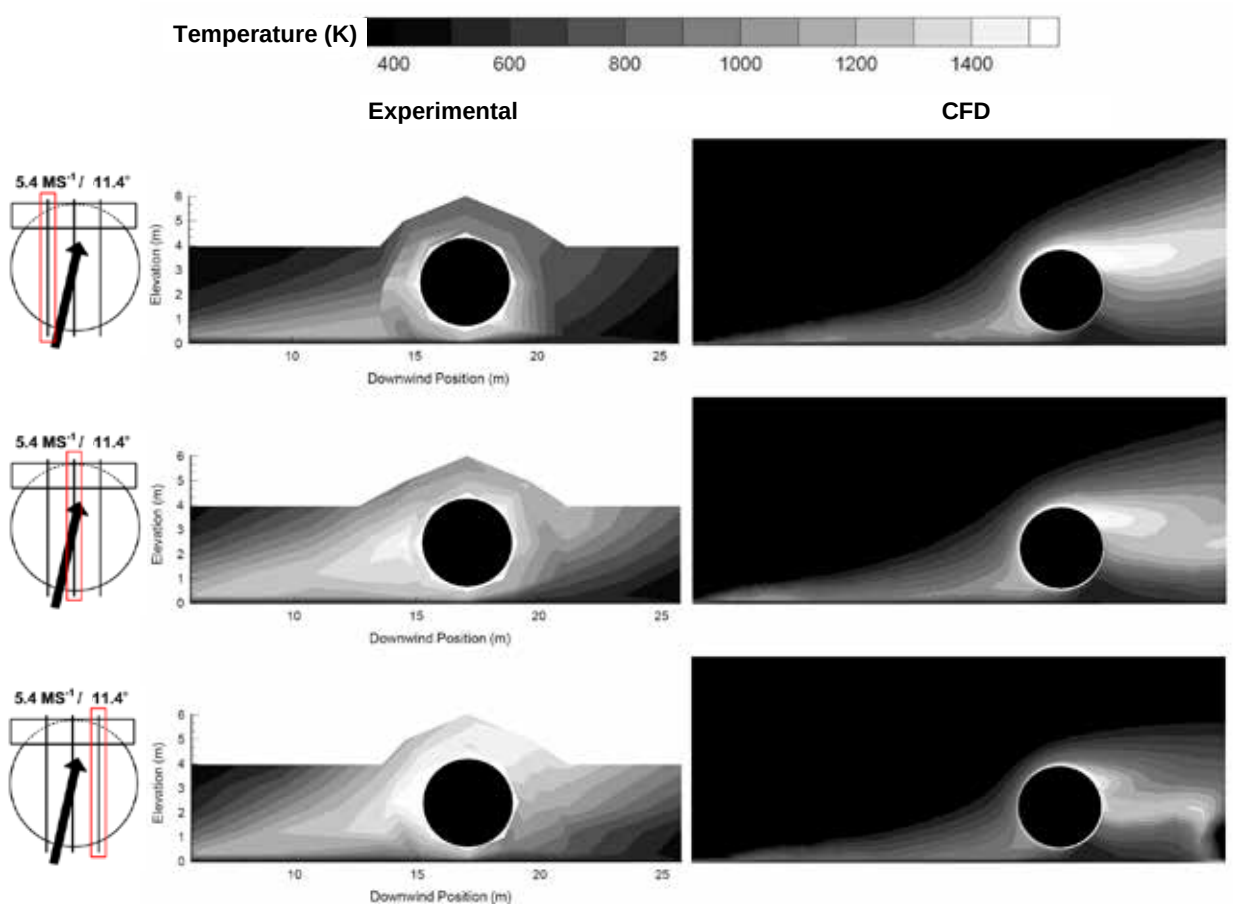

Figure 15. Medium Crosswind Case Showing Flame Temperature Contour Comparisons (Experimental data was adapted from reference 33.)

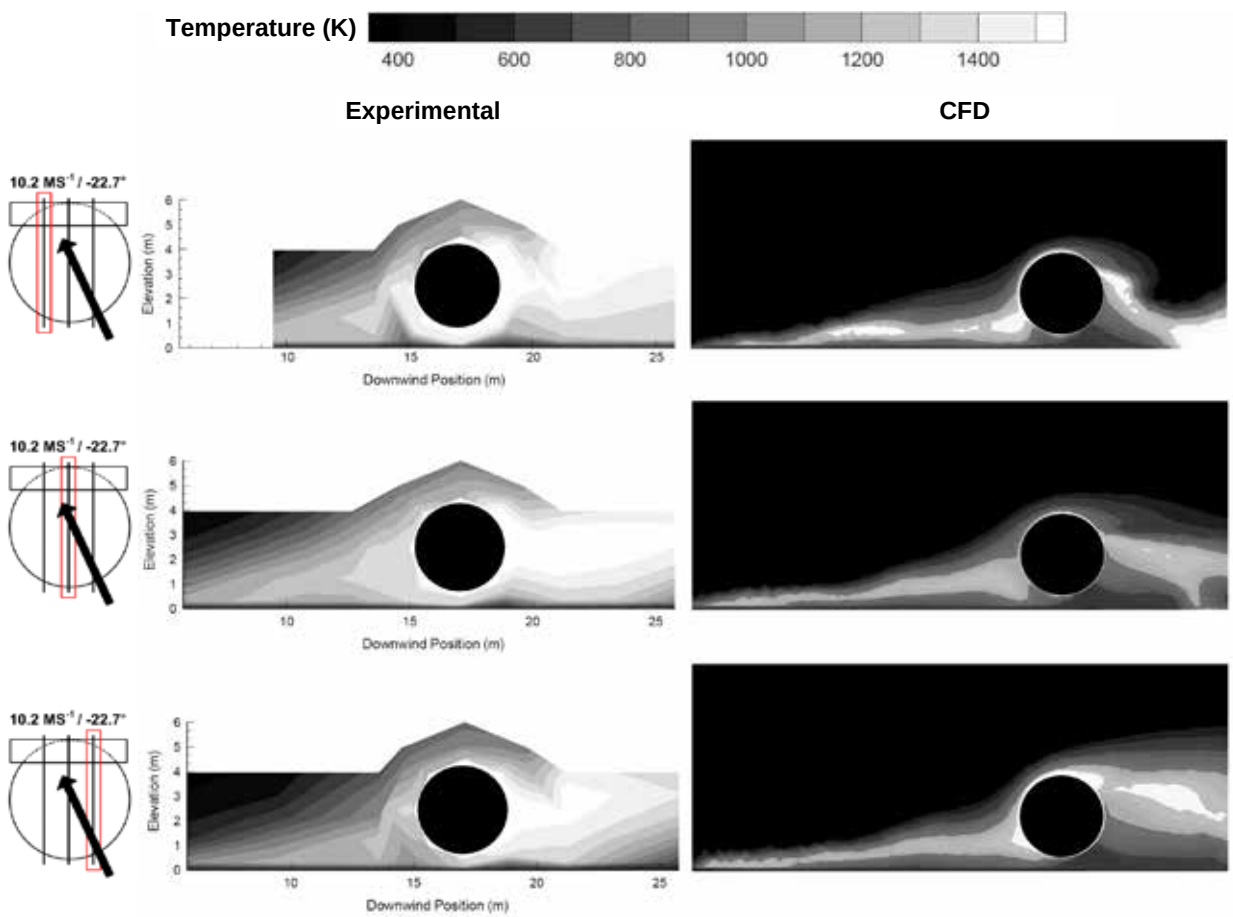

Figure 16. High Crosswind Case Showing Flame Temperature Contour Comparisons (Experimental data was adapted from reference 33.)

3.4.3 Surface Temperatures.

Temperatures were recorded along the mock fuselage surface similar to the way in which flame temperature measurements were taken in section 3.4.2, but instead using surface mount TCs as opposed to standing rakes. Experimental measurements are again aligned on the left, and CFD results are aligned on the right. Mock fuselage surfaces are broken down to the windward and leeward view, annotated by the legend on the far left. Experimental circular fuselage surface data is projected onto a flat surface defined via degrees, and CFD skin data is presented using an orthonormal perspective. A similar scale from 300 K to about 1550 K was implemented to depict surface temperatures.

Figures 17, 18, and 19 report mock fuselage surface temperatures for the low, medium, and high wind speed cases, respectively. Local surface temperatures for all three cases reflect similar results reported in the mock fuselage near field local flame temperatures documented in section 3.4.2. Surface temperatures show good agreement for the low and medium crosswind cases, with significant divergence in comparing the high wind speed experimental and CFD case for the same postulated reasons mentioned at the end of section 3.4.2.

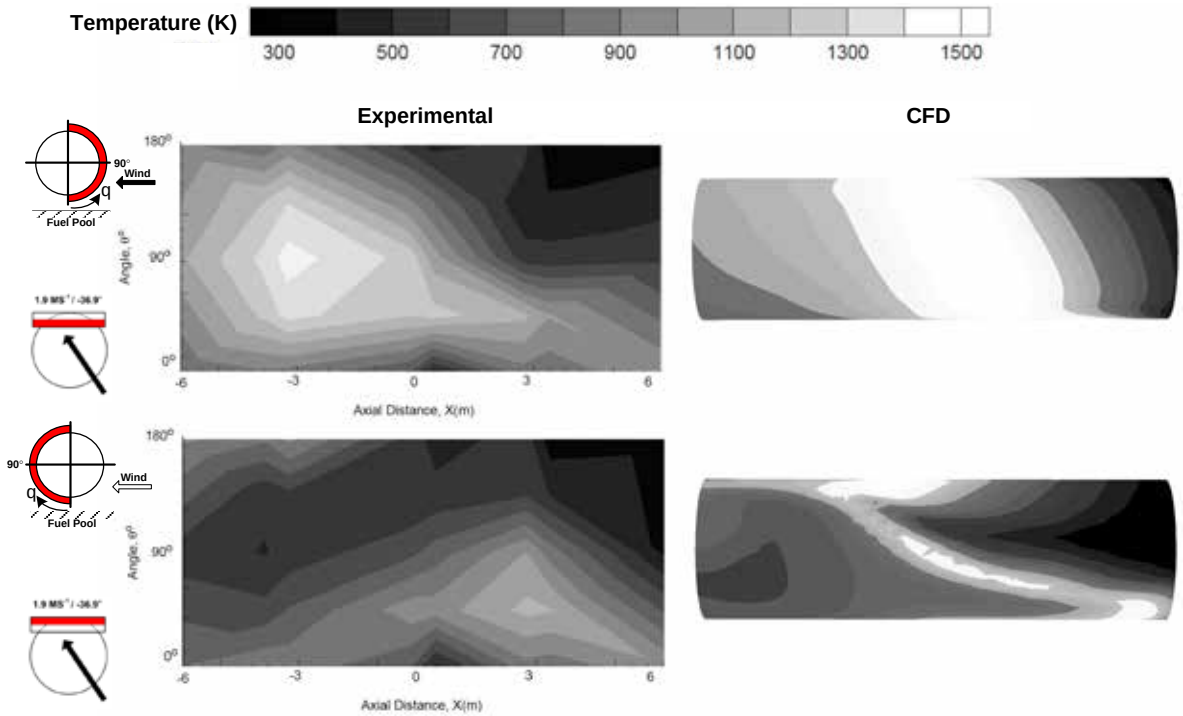

Figure 17. Low Crosswind Case Showing Mock Fuselage Surface Temperature Contours Comparisons (Experimental data was adapted from reference 33.)

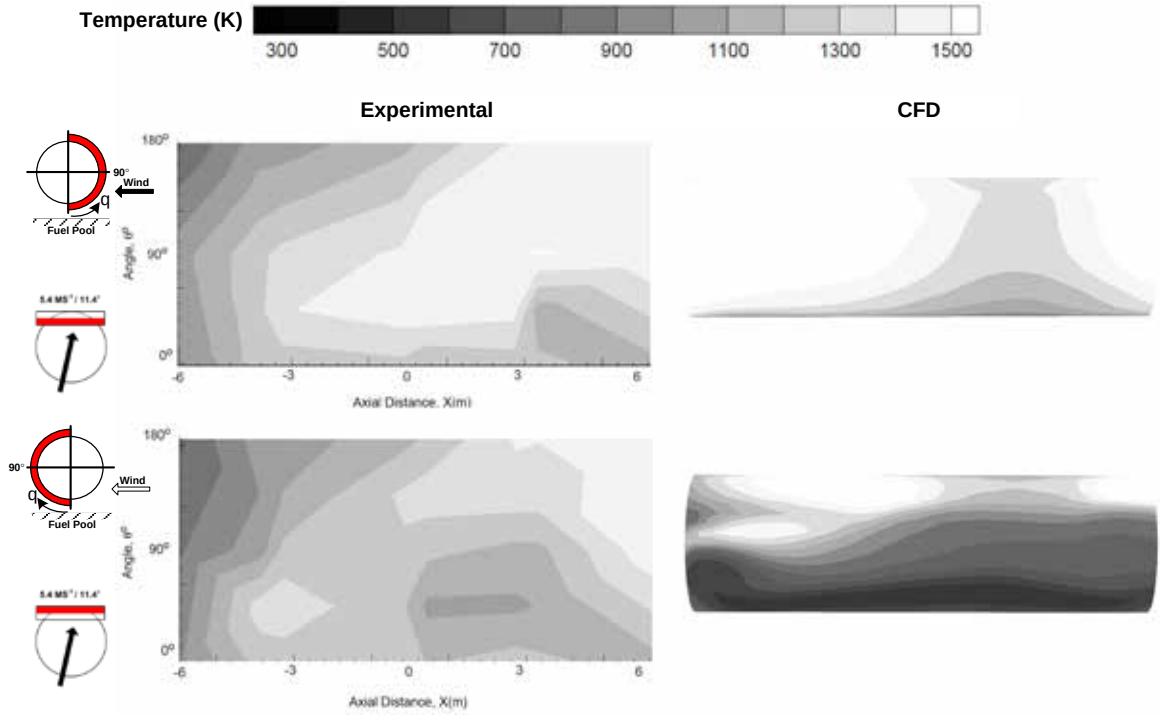

Figure 18. Medium Crosswind Case Showing Mock Fuselage Surface Temperature Contour Comparisons (Experimental data was adapted from reference 33.)

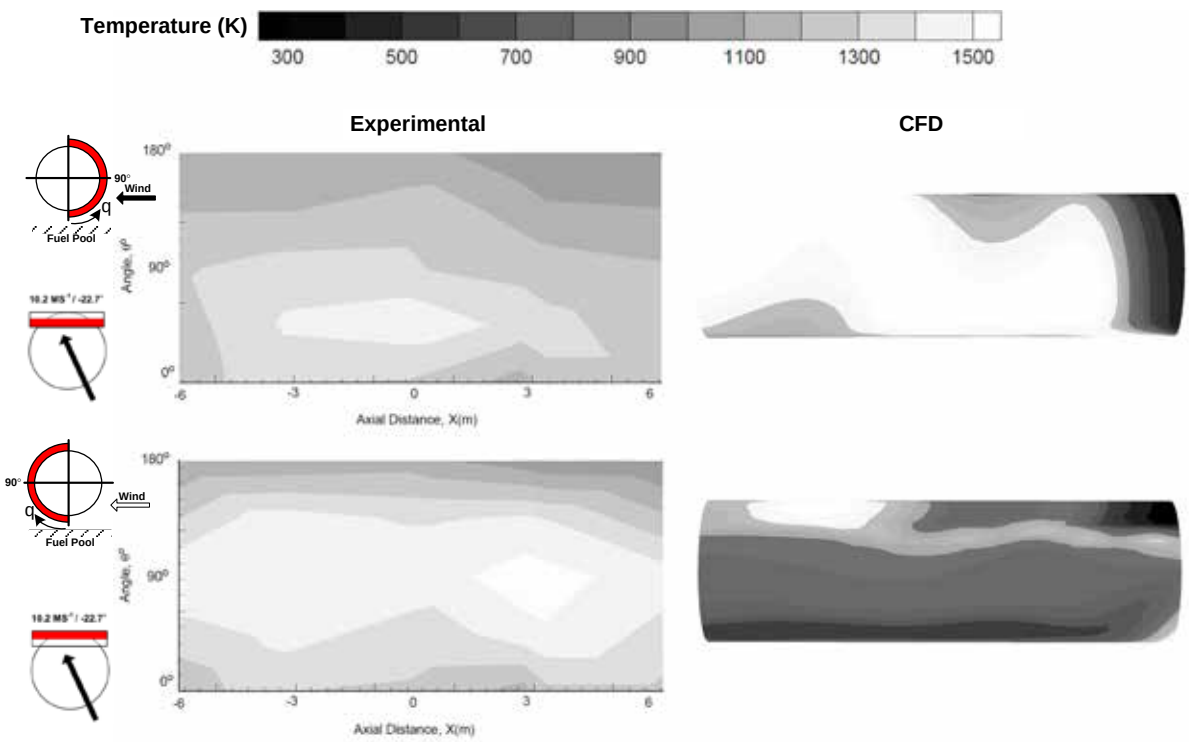

Figure 19. High Crosswind Case Showing Mock Fuselage Surface Temperature Contour Comparisons (Experimental data was adapted from reference 33.)

3.4.4 Surface Heat Fluxes.

Heat flux was recorded along the mock fuselage surface similar to surface temperatures mentioned in section 3.4.3 and appears in figures 20, 21, and 22. The same data presentation methods were used. A single scale from approximately 5 to 230 $kW \times m^{-2}$ was used for the low crosswind case in figure 20, and 40 to 310 $kW \times m^{-2}$ was used for the medium and high crosswind cases to clarify the higher recorded heat fluxes at higher crosswind conditions in figures 21 and 22, respectively. Surface heat flux showed significant gains experimentally as crosswind increased for the low and medium wind speed cases and diverged for the high wind speed case. Similar conclusions were reached for heat flux comparisons as the flame and surface temperatures.

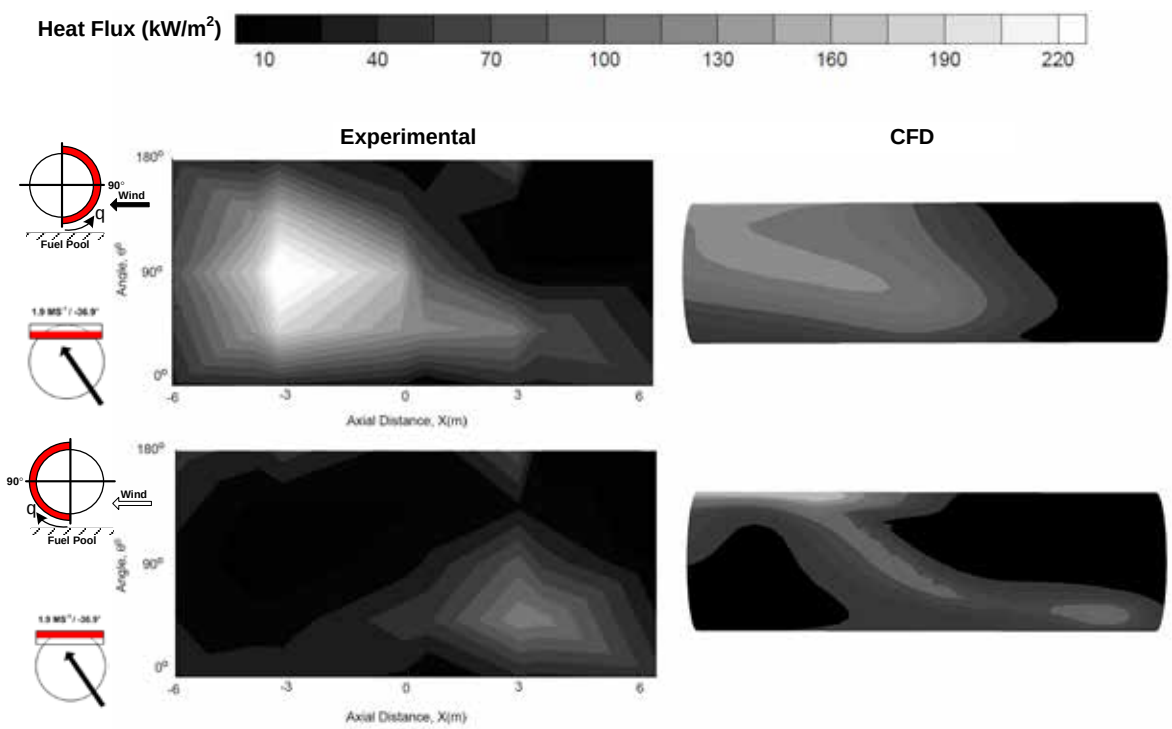

Figure 20. Low Crosswind Case Showing Mock Fuselage Surface Heat Flux Contour Comparisons (Experimental data was adapted from reference 33.)

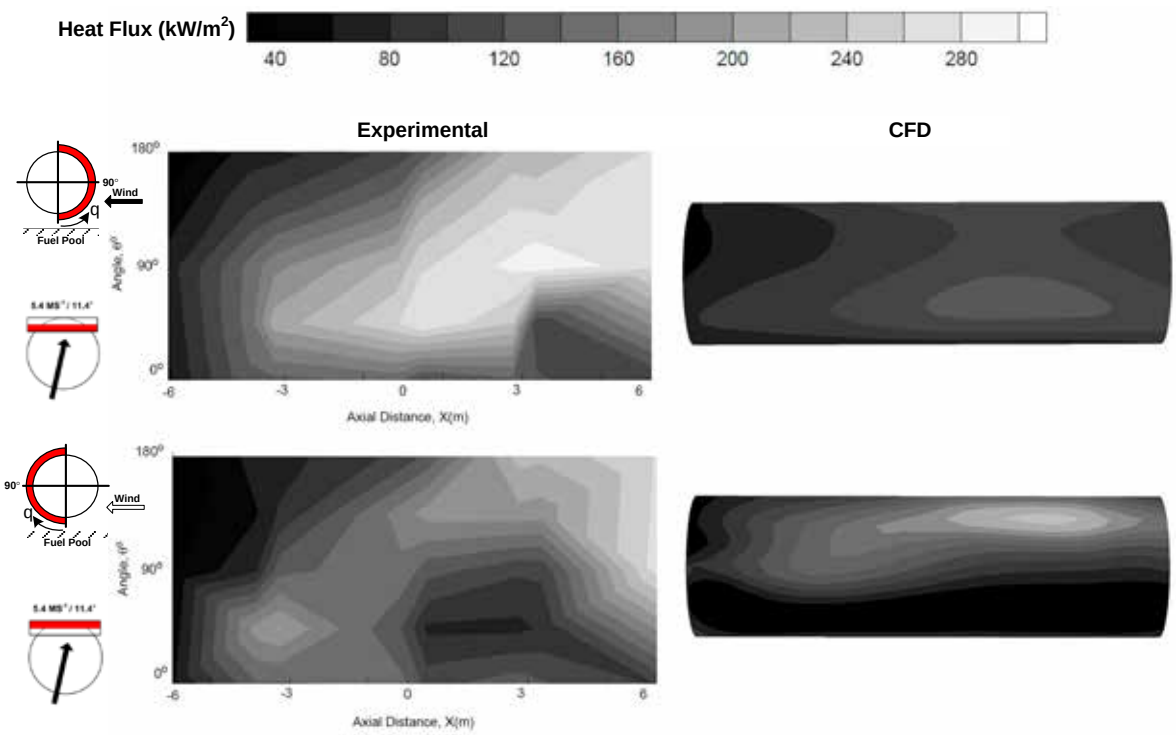

Figure 21. Medium Crosswind Case Showing Mock Fuselage Surface Heat Flux Contour Comparisons (Experimental data was adapted from reference 33.)

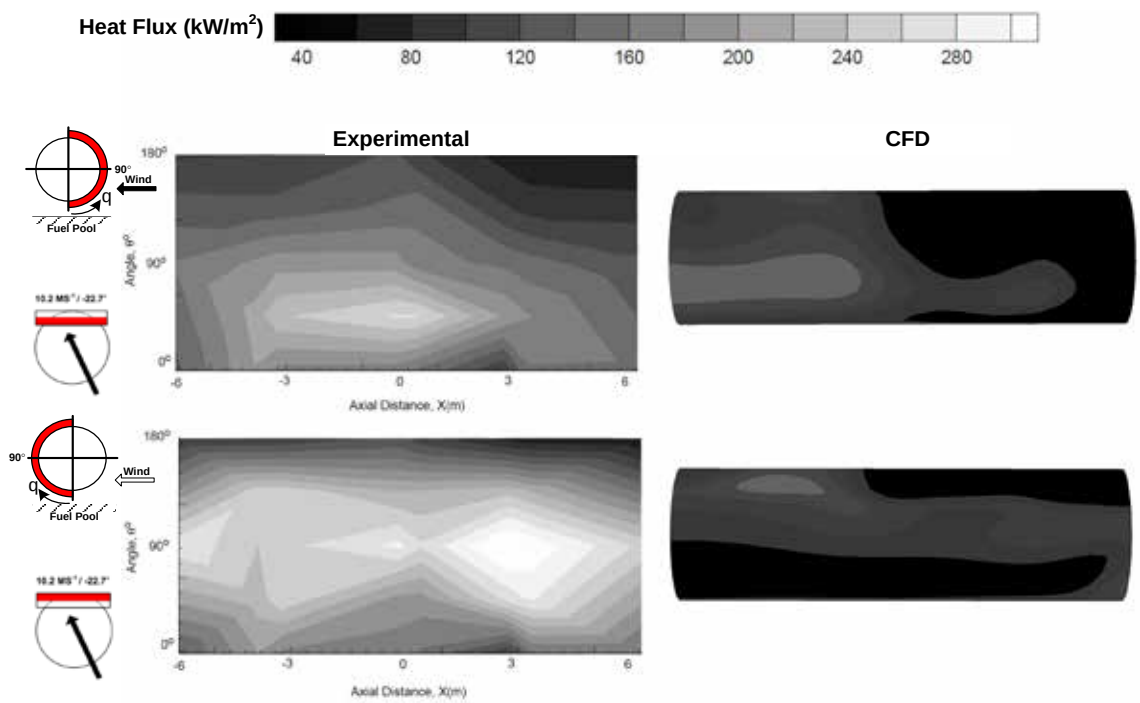

Figure 22. High Crosswind Case Showing Mock Fuselage Surface Heat Flux Contour Comparisons (Experimental data was adapted from reference 33.)

3.4.5 Flow Visualization.

Color contour temperature plots showing the fuel pool surface, mock fuselage, and three cross-sectional planes are depicted for all three crosswind cases in figure 23. Low crosswinds exhibit the lowest temperatures due to minimal fuel-air mixing combined with the most acute wind direction with respect to the mock fuselage. Medium crosswinds had the largest wind fluctuations supporting greater fuel-air mixing. High crosswinds had the least amount of wind fluctuations but the strongest mean flow creating a more aggressively stretched wake region.

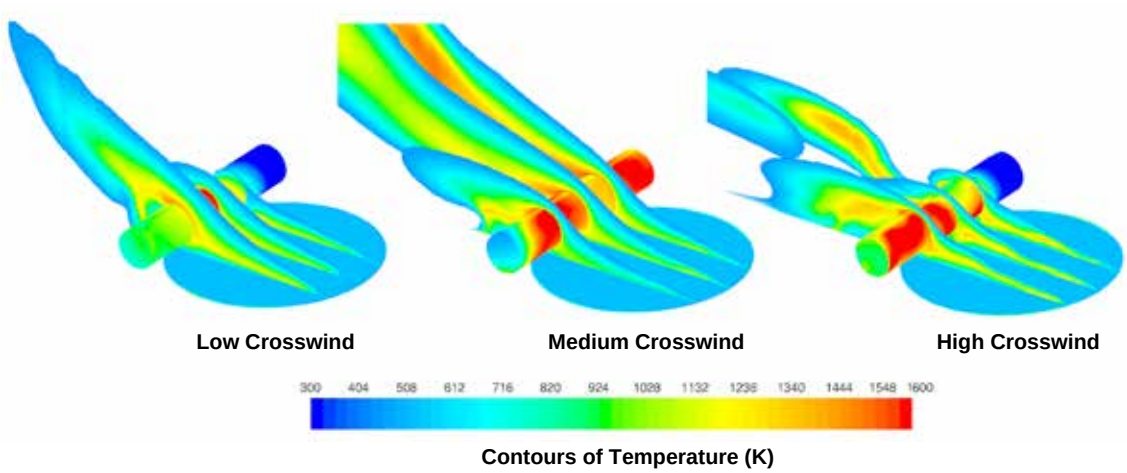

Figure 23. Flame and Surface Contour Temperatures for the Case CFD Validation Case Studies

4. AIRCRAFT COMPUTATIONAL ANALYSIS.

4.1 OVERVIEW.

Three aircraft geometries were selected to analyze relative thermal responses to similar jet fuel pool fire conditions. Low and moderate crosswind conditions with 10% free-stream TI were imposed in the direction normal to each aircraft fuselage to approximate atmospheric conditions. These settings were selected based upon good agreement with experimental data for those respective flow regimes. The B-707-320B was selected to represent the physical features of a traditional airliner in terms of size and shape. The B-777-200ER was one of two NLA designs chosen due to its large frame classification in addition to its circular cross-sectional fuselage and twin-engine build. The third airframe analyzed was the NLA A380-800 equipped with four engines and uniquely identified by its elliptically shaped hull. For brevity, aircraft will be referred to by their family name.

The National Fire Protection Association (NFPA) 403 practical critical area (PCA) fire scenario was the standard chosen for comparison because it provided a well-established geometric basis to generate similar scale aircraft fires. It is formulated from the following relationship:

$$PCA = 0.67 \times [L \times (K + W)] \tag{1}$$

where L, W, and K are the aircraft length, fuselage width, and a constant based upon L, respectively [1]. Figure 24 relates aircraft position to PCA. Table 4 provides relative area statistics of each aircraft fire environment, and table 5 summarizes aircraft fuel capacity and passenger limitations dependent upon internal cabin configuration [51–53]. It should be noted here that aircraft PCA, fuel, and passenger capacity do not scale proportionally. Figures 25 and 26 show multiple views of each aircraft and their unique PCA scaled relative to one another. The same geometries were also used for CFD physical domain construction.

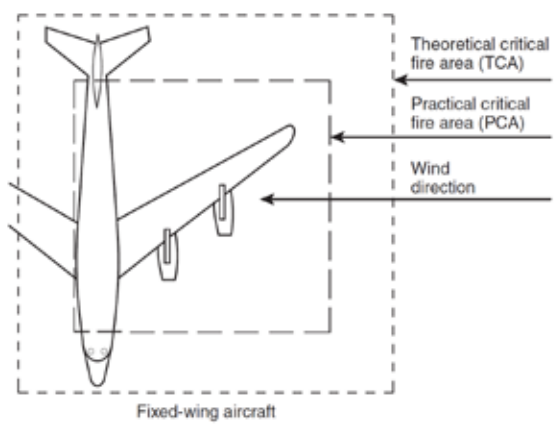

Figure 24. The PCA Size and Location With Respect to the Aircraft
(Adapted from reference 1.)

Table 4. A Summary of Aircraft Wetted Surface and PCA Ratios

Aircraft	Surface Area (m^2)	PCA (m^2)	Ratio (-)
B-707	1252	1054	1.19:1
B-777	2341	1545	1.51:1
A380	3975	1784	2.23:1

Table 5. A Summary of Aircraft Fuel Capacity and Passenger Limitations [51-53]

Aircraft	Fuel Capacity (l)	Passenger Limit*
B-707[51]	90,290	147 or 202
B-777[52]	171,170	301 or 400 – 440
A380[53]	323,546	525 or 853

*Configuration Dependent

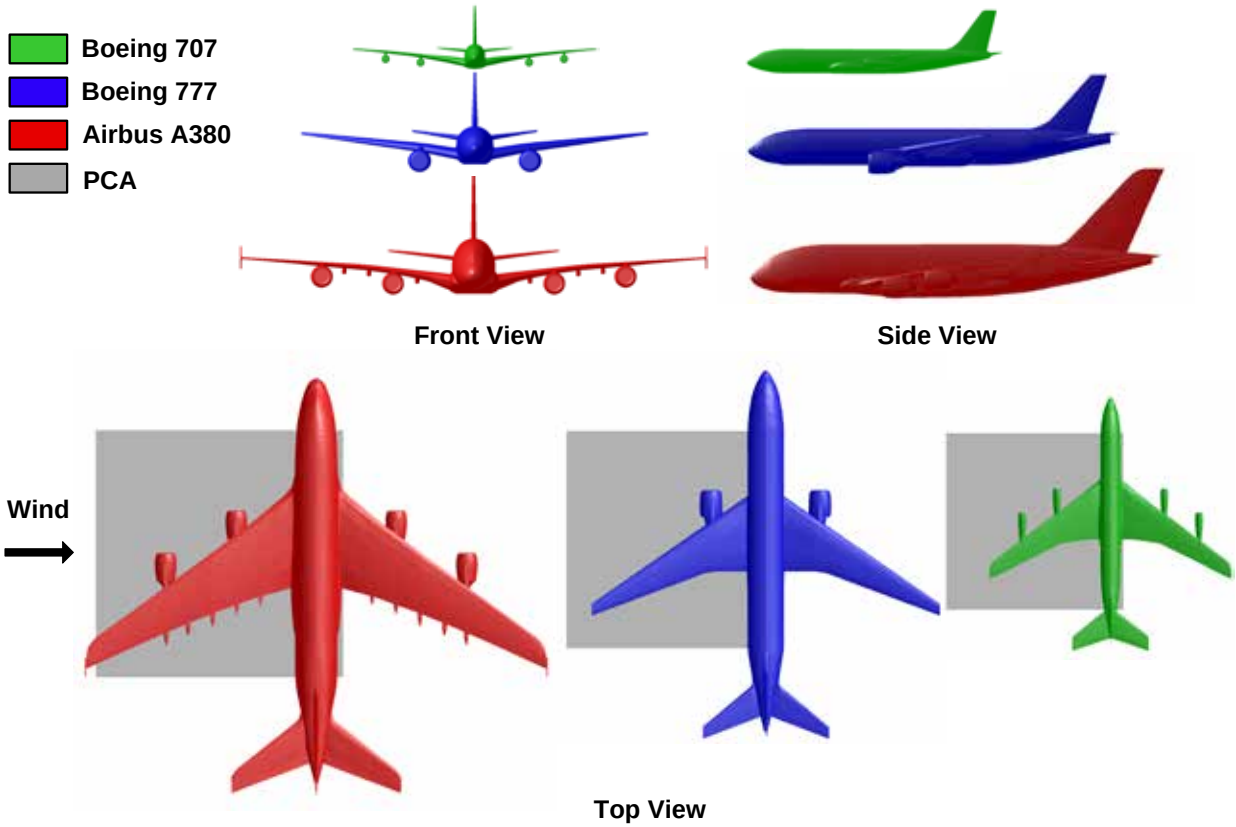

Figure 25. A Comparison of the Relative Scale and Shape Between Each Aircraft

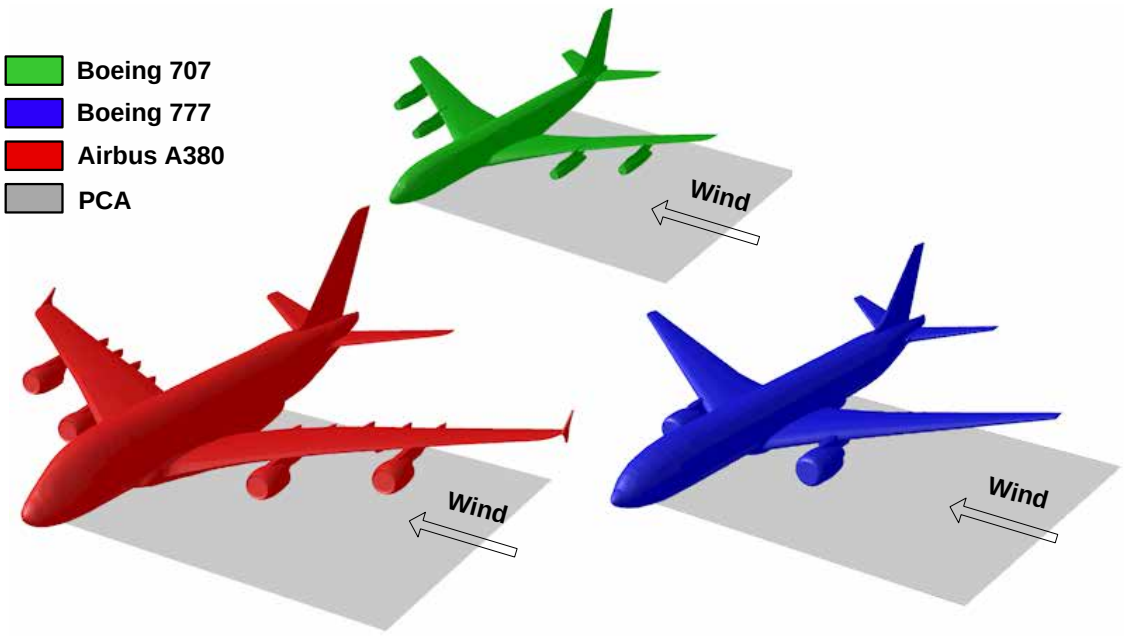

Isometric View

Figure 26. An Alternative Perspective Comparing the Relative Scale and Shape Between Each Aircraft

4.2 PHYSICAL DOMAIN.

Flow domains for all three aircraft were composed similarly to the computational validation studies. A maximum average surface mesh spacing of 10 cm was applied to each aircraft, with areas of high curvature more finely resolved. Mesh sizes ranged from 9.5 (B-707) to 10.9 (A380) million cells. Figure 27 depicts various aspects of the A380 geometric mesh.

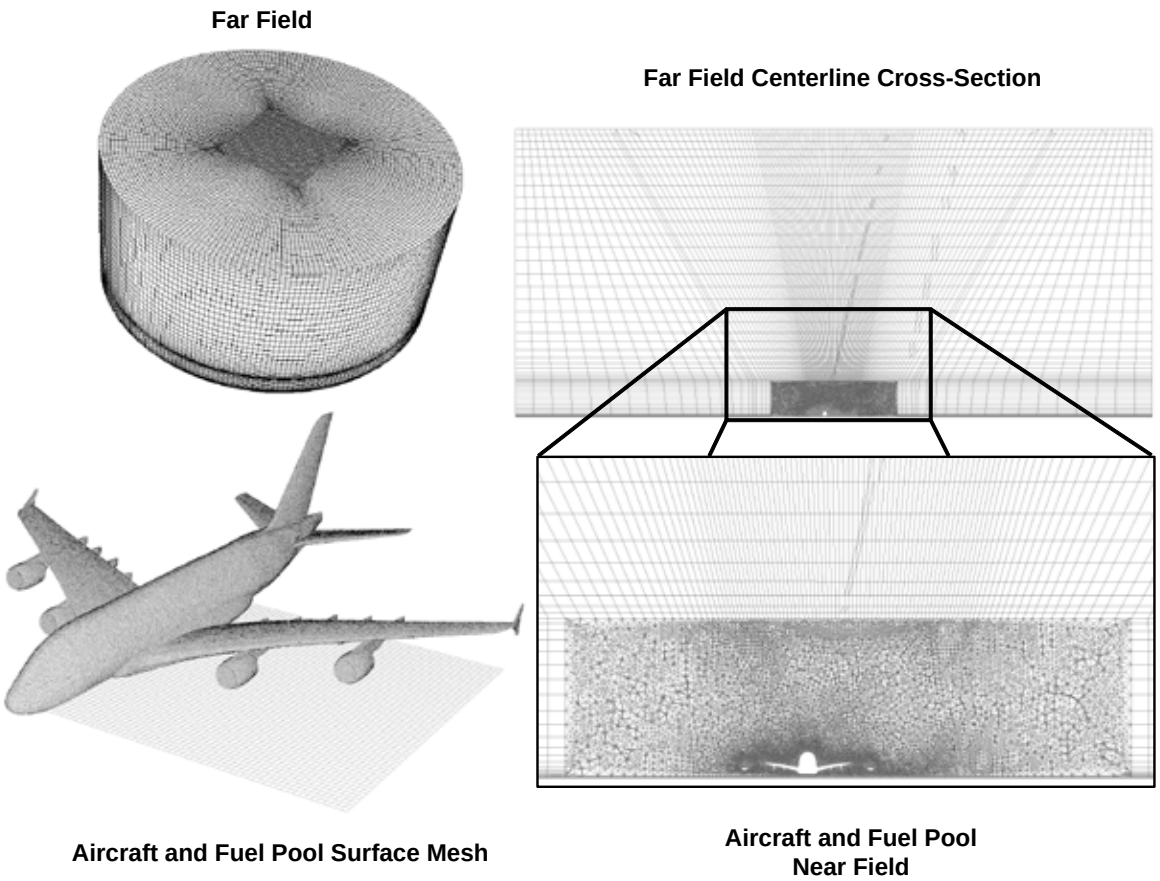

Figure 27. The A380 Geometric Mesh

4.3 BOUNDARY CONDITIONS.

Boundary conditions for each aircraft analysis were imposed similarly to the validation studies. The aircraft surface was treated in the same manner as the mock fuselage surface, and the PCA was treated in a similar manner as the pool fire zone by extrapolating the fuel recession mass flow rate to compensate for the increase in area. Free-stream conditions and surrounding ground area were treated identically.

4.4 RESULTS.

Steady-state as well as time-accurate simulations using a 50-ms fixed time step over a 120-s period were calculated for each of the three aircraft exposed to low (2 $m \times s^{-1}$) and medium (5 $m \times s^{-1}$) crosswind conditions. Unsteady calculations were initialized from the steady-state solution allowing 30 s of transition to fully developed unsteady flow. All cases were executed on a Department of Defense Supercomputing Resource Center SGI® Altix® ICE. Hardware utilization consisted of 64 Nehalem Intel® Xeon® processor cores connected via InfiniBand™. Each simulation took approximately 4000 CPU hours (about 60 real-time hours) to complete.

4.4.1 Surface Temperatures and Heat Fluxes.

Aircraft surface thermal response was a critical factor recorded for each time step to interpret dynamic aircraft-fire interaction. Figure 28 shows transient mean temperatures and heat fluxes averaged over the entire aircraft surface during a fully developed 60-s unsteady period exposed to low and medium crosswinds. Results indicated that low crosswinds allow the periodic mean fire plume pulsations to dominate heat transfer to the aircraft. Conversely, medium crosswind conditions force a higher rate of aircraft-plume interaction resulting in faster secondary flow structures. This causes increased turbulent fuel-air mixing and greater heat transfer. Table 6 shows a quantitative comparison of the mean thermal response between each aircraft; this comparison shows heat transfer magnitudes approximately doubling between low and medium crosswinds conditions, a trend established during the CFD validation study. Percent differences are calculated relative to the B-707. It is further speculated that as crosswind magnitudes increase, overall heat transfer becomes increasingly independent of secondary changes in aircraft geometry (fuselage shape, engine layout, wing planform, etc.) as long as the mean wake structure created by the aircraft body is not significantly altered.

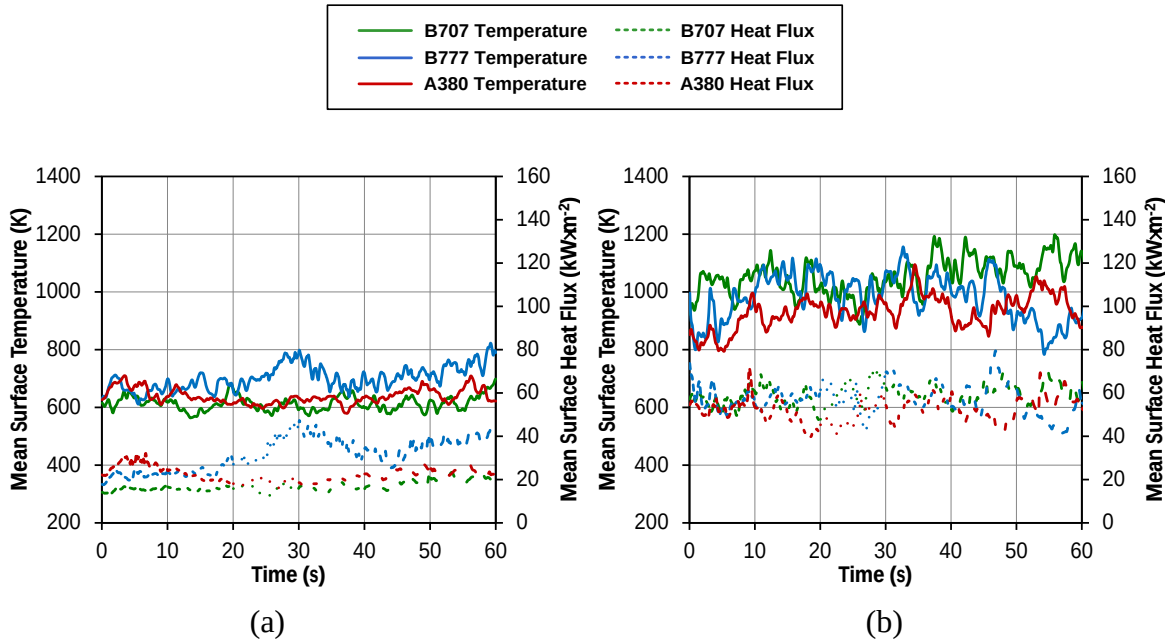

Figure 28. Comparisons of Mean Aircraft Surface CFD Temperatures and Heat Fluxes Exposed to (a) Low and (b) Medium Crosswinds

Table 6. A Summary of Time-Averaged Mean Aircraft Surface Thermal Signatures

Aircraft	Mean ± RMS Temperature (K)	Difference (%)	Mean ± RMS Heat Flux ($kW \times m^{-2}$)	Difference (%)
Low Crosswind				
B-707	613 ± 25	--	16.8 ± 2.9	--
B-777	701 ± 42	14.4	31.4 ± 7.5	86.9
A380	639 ± 26	4.3	22.4 ± 3.3	33.3
Medium Crosswind				
B-707	1050 ± 65	--	59.7 ± 4.9	--
B-777	957 ± 82	8.6	55.6 ± 6.5	6.9
A380	949 ± 58	9.6	52.3 ± 5.1	12.4

Figures 29 through 32 illustrate time-averaged aircraft surface temperatures and heat fluxes exposed to medium crosswind conditions for a 60-s period. Aircraft fuselage lengths are normalized for easier interpretation of results. Mean temperatures peaked at approximately 1200 K, and mean heat fluxes peaked at about 100 $kW \times m^{-2}$. RMS temperatures fluctuated between 10% and 70% of the time-averaged value. Low crosswind results depicted similar contour profile trends but at lower magnitudes, as quantified in table 6.

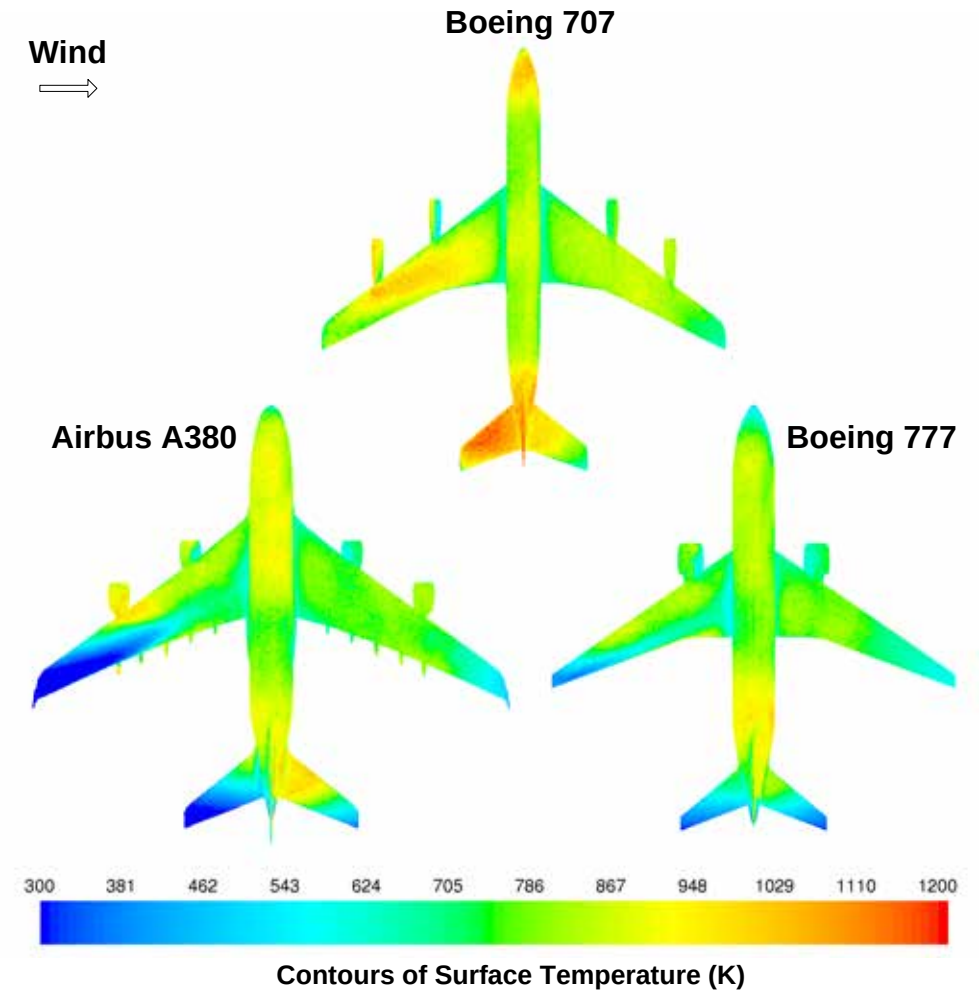

Figure 29. Top View of Time-Averaged Aircraft Surface Temperatures Exposed to Medium Crosswinds

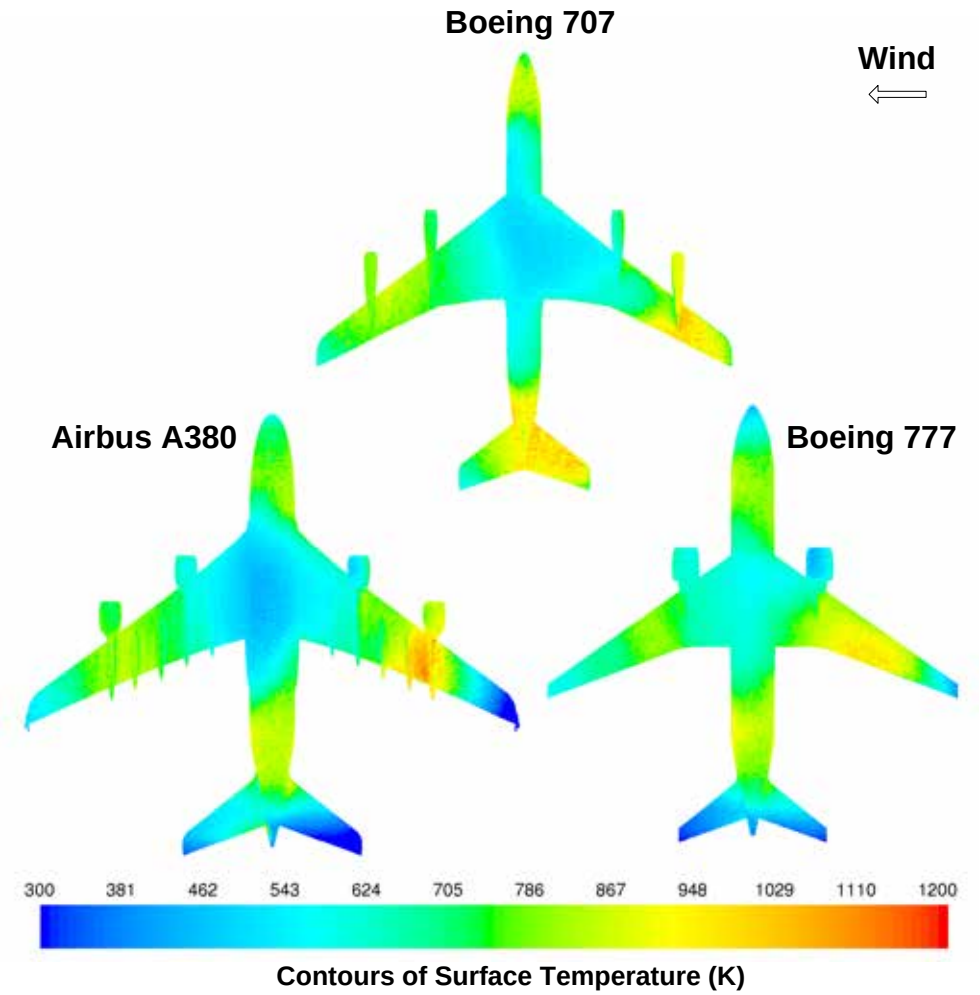

Figure 30. Bottom View of Time-Averaged Aircraft Surface Temperatures Exposed to Medium Crosswinds

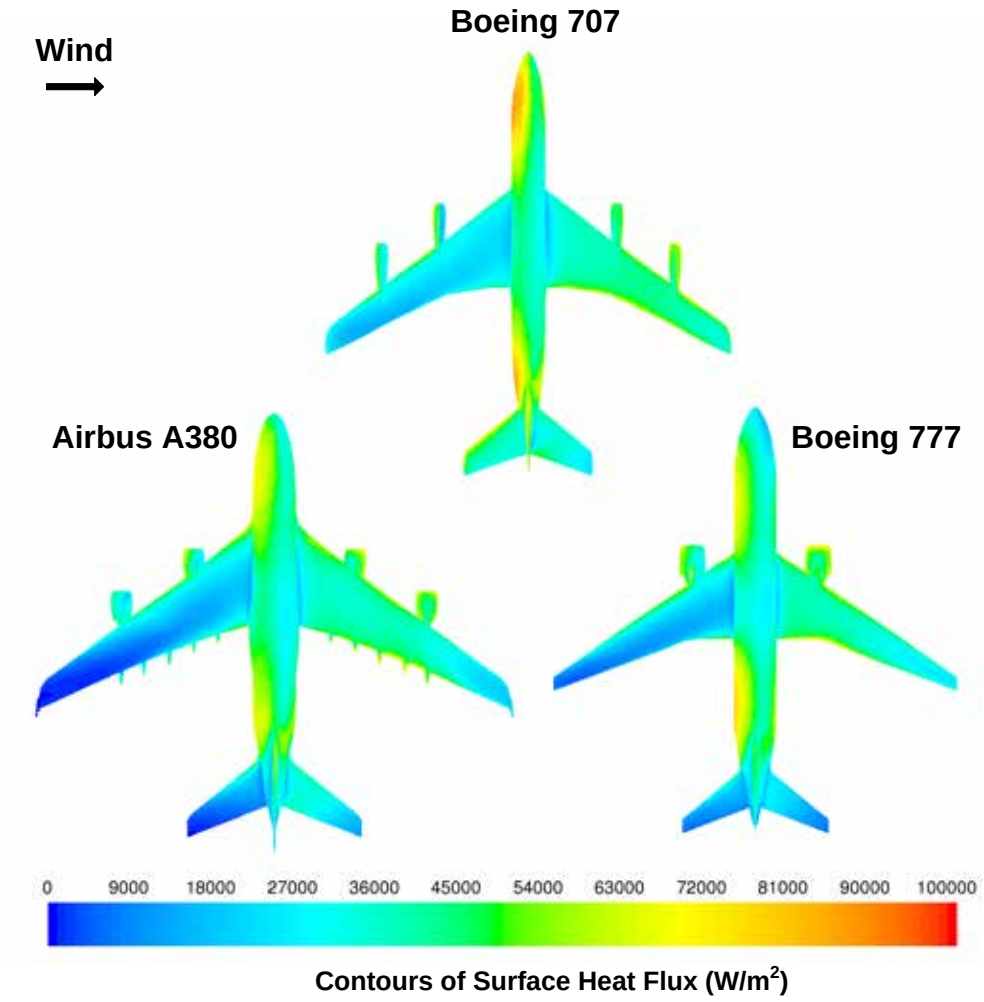

Figure 31. Top View of Time-Averaged Aircraft Surface Heat Flux Exposed to Medium Crosswinds

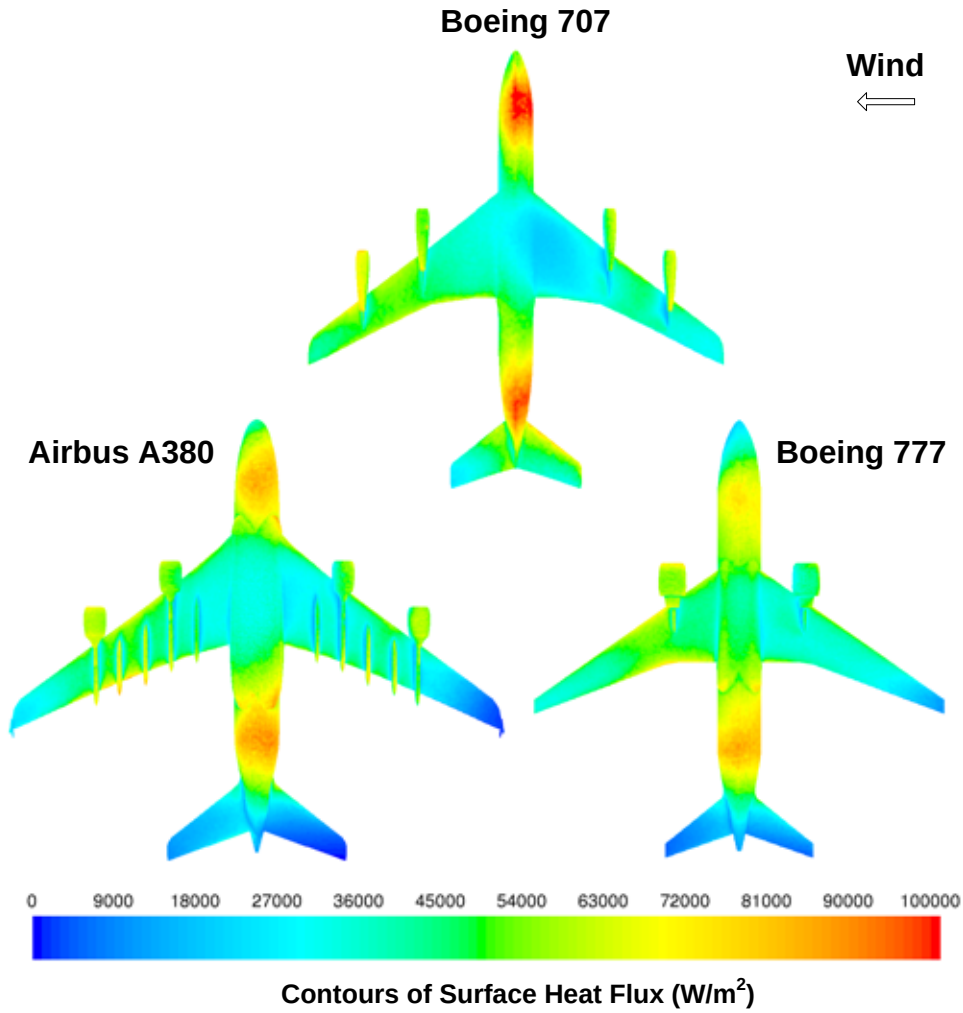

Figure 32. Bottom View of Time-Averaged Aircraft Surface Heat Flux Exposed to Medium Crosswinds

Certain locations exhibited strong three-dimensional flow effects such as around engine nacelles, the fuselage nose, and horizontal and vertical stabilizers. These locations that also existed in the flame zone generated enhanced heat transfer due to greater turbulent fuel-air mixing and more exposure to entrained air. Areas in close proximity to the ground and central to the body were exposed primarily to more oxygen-starved, fuel-rich conditions reducing local heat transfer.

Near-field time-averaged aircraft surface and PCA fuel pool temperatures are shown in figures 33 and 34, which depict the time-averaged effect of the aircraft-fire plume interaction on the surrounding area. Enhanced areas of heat transfer along fuel-air interfaces are identified. Three-dimensional heat transfer effects are also more easily observed. Increases in surface temperature in the near-field ground area are attributed to the crosswind flow constrictions induced by aircraft proximity with the ground. Because the B-707 maintains the lowest overall average ground clearance of all three aircraft, local fuel-air mixing in these regions is enhanced causing the largest rise in temperature.

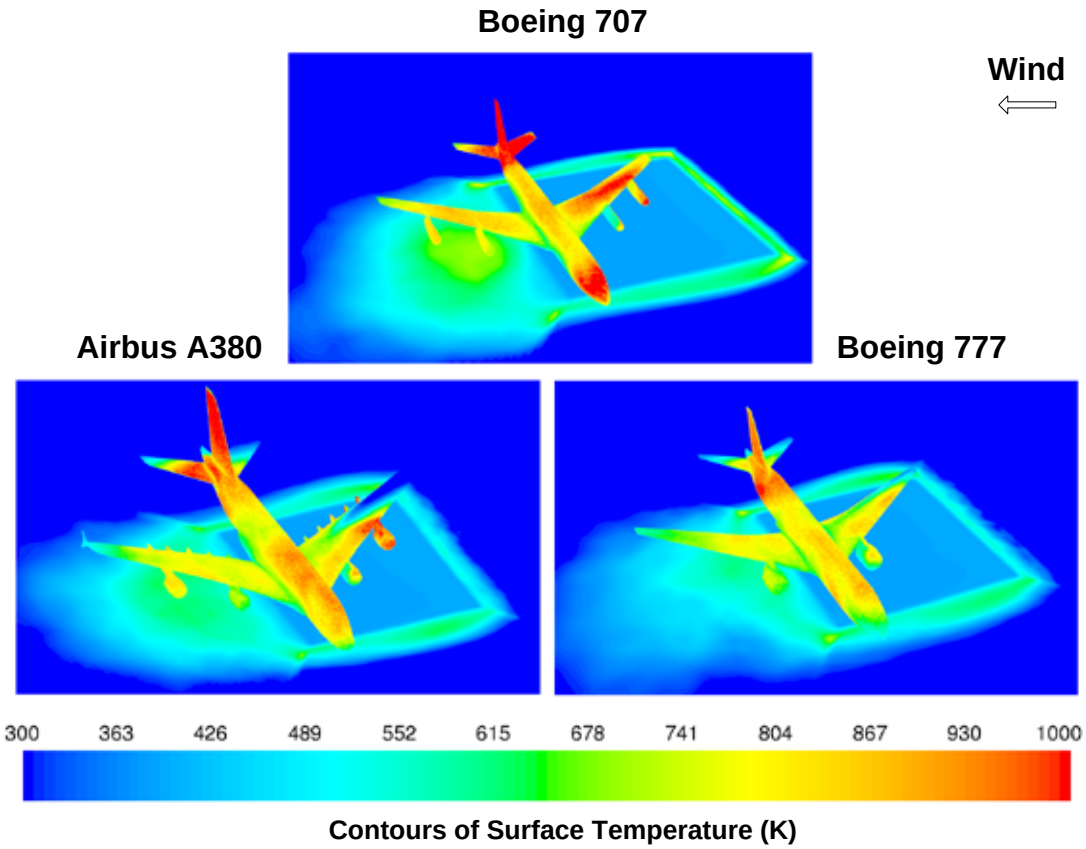

Figure 33. Time-Averaged Near-Field Aircraft Surface Fuel Zone and Ground Temperatures Exposed to Medium Crosswinds (Isometric View)

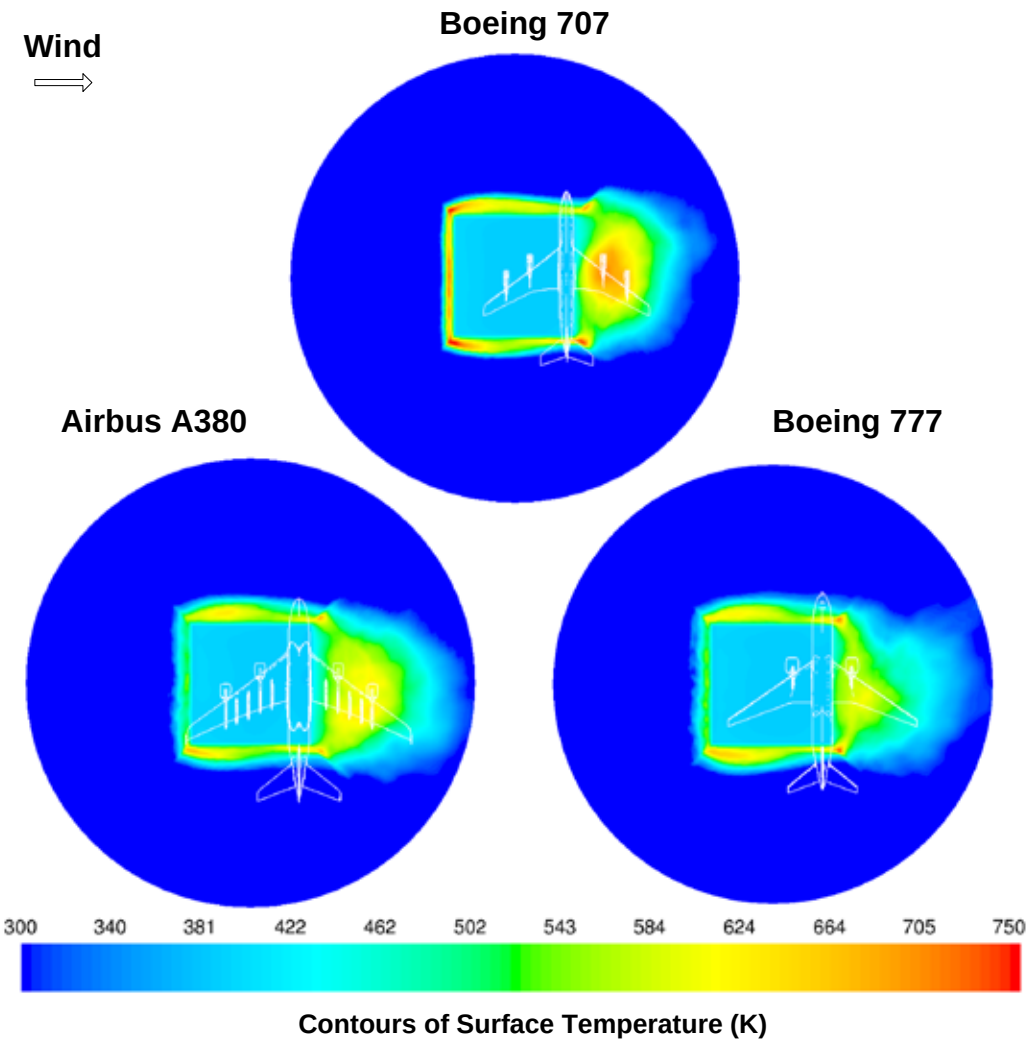

Figure 34. Time-Averaged Near-Field Ground and Fuel Surface Temperatures Exposed to Medium Crosswinds (Top View)

4.4.2 Flame Temperatures.

Figures 35 and 36 show time-averaged flame temperatures from both far- and near-field perspectives, respectively. Radial temperature profiles emanating from the fire plume center compared well among all three aircraft, increasing in width as PCA increased and showing peak flame temperatures of approximately 1000 K. Figure 35 also shows mean flame height also increased with the base fire size.

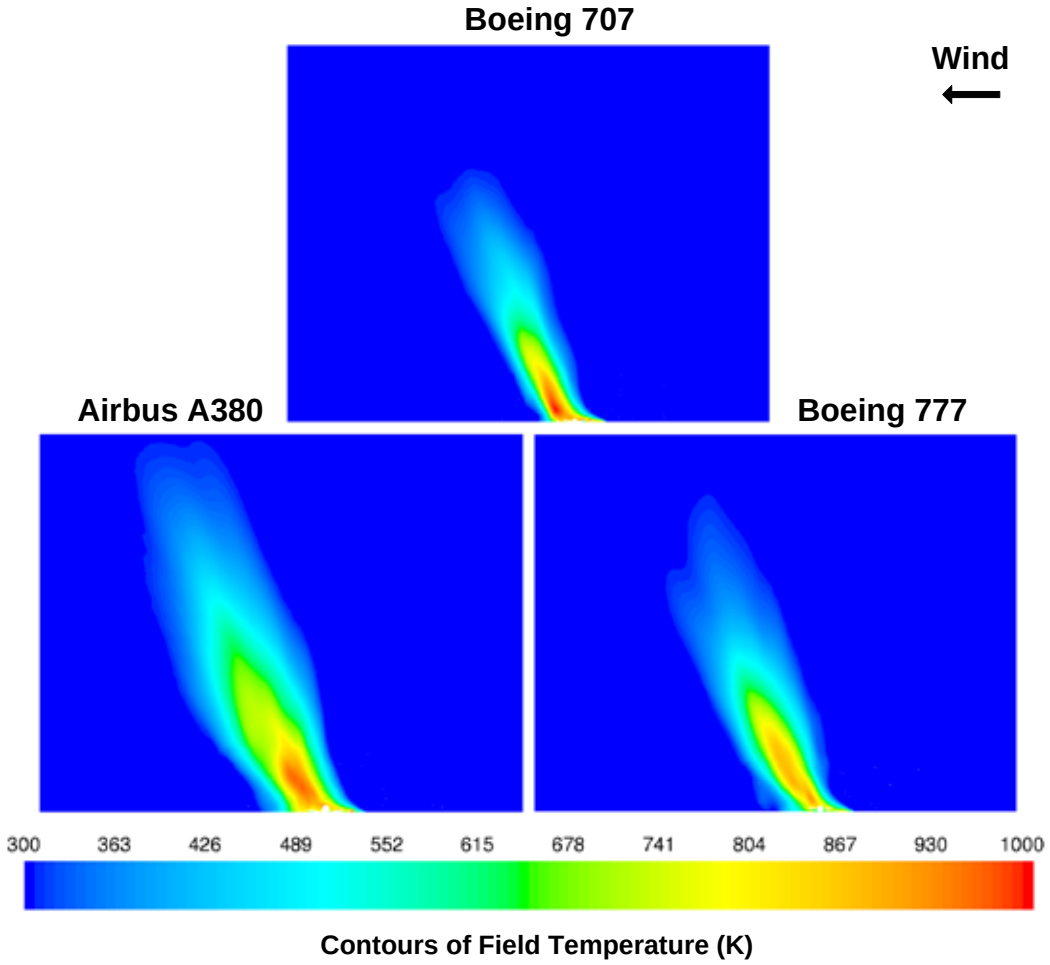

Figure 35. Time-Averaged Far-Field Fire Plume Temperatures Exposed to Medium Crosswinds (Front View)

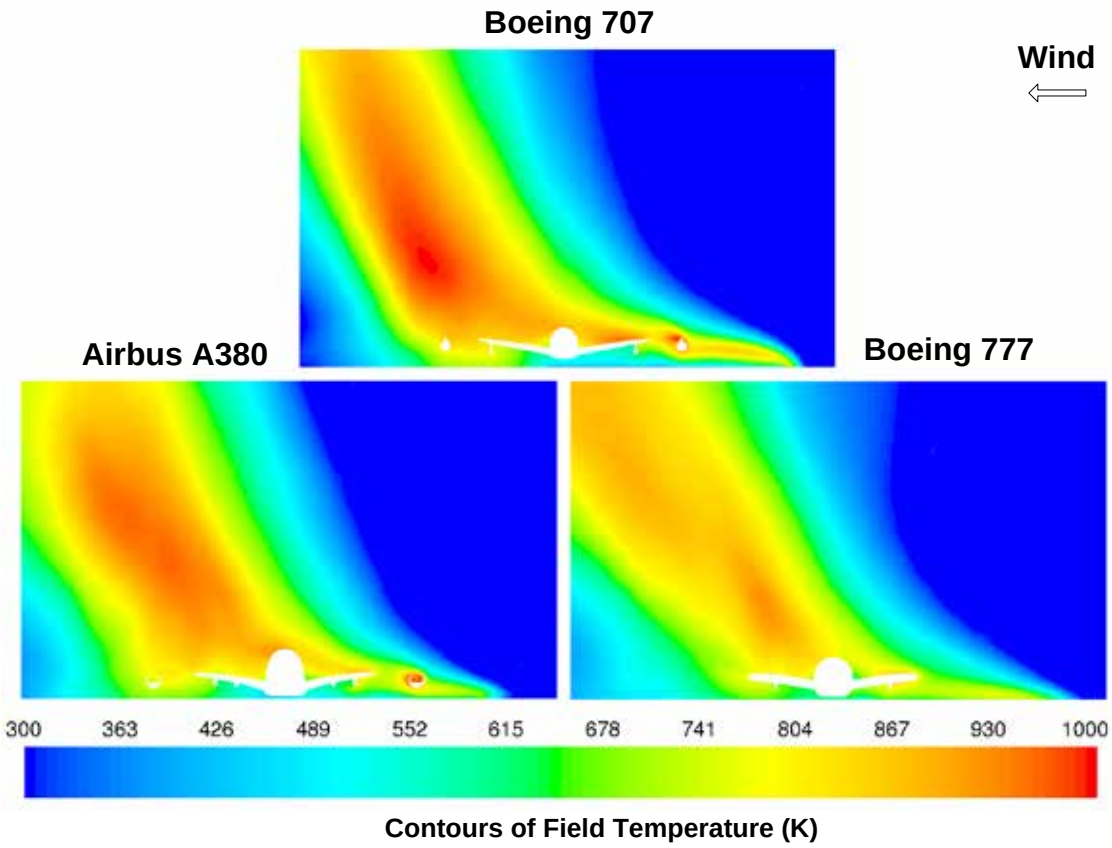

Figure 36. Time-Averaged Near-Field Fire Plume Temperatures Exposed to Medium Crosswinds (Front View)

4.4.3 Flame Velocities.

Figure 37 shows the same reference frame as figure 34 illustrating far-field fire plume velocity magnitudes for each aircraft exposed to medium crosswinds. Similar to flame height and width, core flame velocities increased with increasing PCA, and peak magnitudes of approximately 35 $m \times s^{-1}$ were calculated.

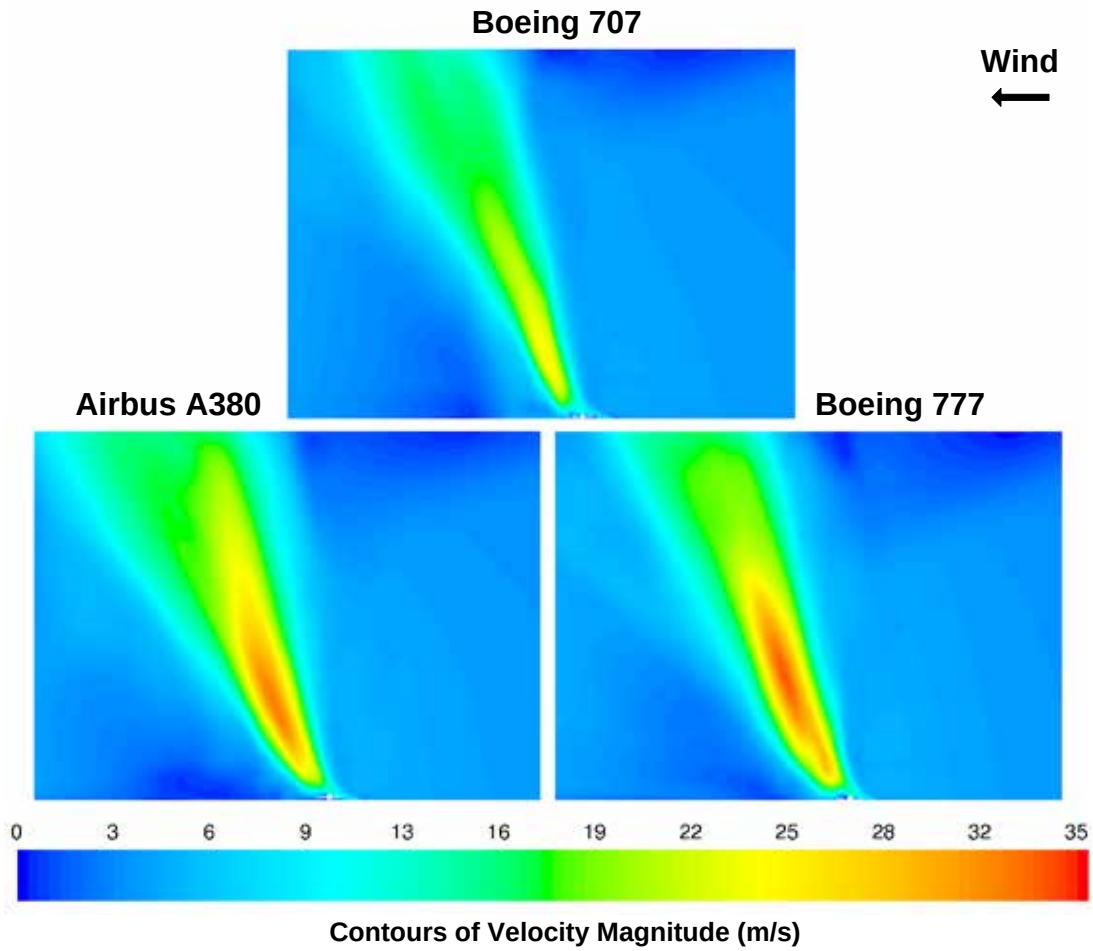

Figure 37. Time-Averaged Far-Field Fire Plume Velocity Magnitudes Exposed to Medium Crosswinds (Front View)

5. CONCLUSIONS.

A computational aircraft pool fire model was developed capable of predicting the major combustion plume features and heat transfer magnitudes to immersed objects exposed to low and medium atmospheric crosswind conditions. Computational fluid dynamic (CFD) results supported experimental measurements that as wind velocity increases, turbulent fuel-air mixing is enhanced, which results in increased heat transfer to bodies engulfed in the flame zone. Divergence from experimental data at high crosswinds can likely be attributed to multiple factors involving the breakdown of turbulence and combustion model assumptions. Discrepancies at lower crosswind conditions are likely attributed to inconsistencies related to quasi-steady state flow assumptions along with simplifications made in generating experimental flame zone planes for comparison to CFD. To increase accuracy, higher-fidelity Large-Eddy Simulation (LES) turbulence models were examined, but they exhibited little improvement over mean and root mean square thermal signatures already calculated and well validated using Reynolds-Averaged Navier-Stokes (RANS). Numerical stability also decreased for LES calculations, decreasing overall robustness to the solution process.

Time-averaged aircraft analysis suggested a consistent correlation between different aircraft geometries exposed to the same crosswind conditions when considering fire scenarios proportional to their overall size. As crosswind increased, aircraft thermal response became less dependent upon aircraft geometry due to inertial atmospheric forces driving turbulent fuel-air mixing. For weaker crosswinds, aircraft-fire plume interaction governed heat transfer. Flame dynamics showed similar trends when comparing fire plume velocities and temperatures. Other reasons for minor thermal response differences may be attributed to fire scale similarity misrepresentations by the practical critical area (PCA). This becomes plausible when other characteristics, such as the aircraft wetted surface area, scale more linearly with factors like fuel and passenger capacity.

Overall interpretation of the data infers nominal design changes in aircraft geometry (fuselage shape, wing planform, and engine layout) do not create an extraordinary fire protection threat when exposed to similar scale flame conditions. This holds true for both New Large Aircraft (NLA) as well as traditionally sized aircraft. Although unique instantaneous heat signatures were observed, general trends remained the same. All thermal attributes stayed within the same order of magnitude and, in the majority of instances varied less than 15%, most notably when exposed to higher heat transfer conditions. However, with NLA carrying larger amounts of fuel compared to the majority of commercial passenger carrying aircraft, NLA have the capacity to create a significantly larger accidental fire threat.

As hybrid RANS-LES turbulence modeling techniques gain widespread reliability, they could be considered to improve overall accuracy of the simulation process. Novel meshing techniques, like anisotropic boundary layers to simplify grid topologies along with other mesh-reducing optimizations, could also be implemented as their dependability increases to reach faster solution turnaround times. Multiscale fire scenarios could also be considered for analysis, as sole reliance on PCA similarity could be suspect. In addition, crosswind magnitudes and directions representative of historical fire emergency scenarios could be introduced to integrate real-world metrics into the analysis.

6. REFERENCES.

1. National Fire Protection Association (NFPA), *NFPA 403 Standard for Aircraft Rescue and Fire Fighting Services at Airports*, 2003 edition, NFPA, Quincy, Massachusetts.

2. Gladman, P., "Airbus A380 & Boeing 747-400," Flightglobal/Blogs, Reviewed February 2011, http://www.flightglobal.com/blogs/aircraft-pictures/2008/01/airbus-a380-boeing-747-400.html

3. Patterson, J., "New Large Aircraft Composite Fire Fighting," Airport Technology Research and Development Branch, Reviewed November 2010, http://www.airporttech.tc.faa.gov/safety/bagot2.asp (Note this is an upcoming project that is not currently active.)

4. Wright, J., "Rescue and Firefighting Research Program," FAA report DOT/FAA/AR-00/67, January 2001.

5. Nicolette, V.F., "Computational Fire Modeling for Aircraft Fire Research," Sandia Report, SAND-96-2714, November 1, 1996, Albuquerque, New Mexico.

6. Hamins, A., Kashiwagi, T., and Buch, R., "Characteristics of Pool Fire Burning," *Fire Resistance of Industrial Fluids*, ASTM STP 1284, Totten, G.E. and Reichel, J., eds., American Society for Testing and Materials (ASTM), 1996, Philadelphia, Pennsylvania.

7. Heskestad, G., "Fire Plumes, Flame Height and Air Entrainment," *The SPFE Handbook of Fire Protection Engineering*, 2nd Edition, DiNenno, P.J., et al., eds., 2002, NFPA, Quincy, Massachusetts.

8. Zukoski, E.E., "Properties of Fire Plumes," *Combustion Fundamentals of Fire*, Cox, G., ed., 1995, Academic Press, London.

9. McCaffrey, B., "Flame Height," *The SFPE Handbook of Fire Protection Engineering*, DiNenno, P.J. et al., eds., Section 2: NFPA, Quincy, Massachusetts, 1995.

10. Quintiere, J.G., *Fundamentals of Fire Phenomena*, April 21, 2006, John Wiley & Sons, Sussex, U.K.

11. Steinhaus, T., Welch, S., Carvel, R., and Torero, J.L., "Large-Scale Pool Fires," *Thermal Sciences Journal*, Vol. 13, Issue 13 (special on fire), 2007.

12. Tieszen, S., Nicolette, V.F., Gritzo, L.A., Holen, J.K., Murray, D., and Moya, J.L., "Vortical Structures in Pool Fires: Observations, Speculation, and Simulation," Sandia Report SAND96-2607, November 26, 1996, Albuquerque, New Mexico.

13. Ricks, A.J. and Blanchat, T.K., "Hydrocarbon Characterization Experiments in Fully Turbulent Fires," Sandia Report SAND2007-2391, March 1, 2011, Albuquerque, New Mexico.

14. McGrattan, K.B., Baum, H.R., and Hamins, A., "Thermal Radiation From Large Pool Fires," National Institute of Standards and Technology (NIST) Report, NISTIR 6546, November 2000, Gaithersburg, Maryland.

15. Brabrauskus, V., "Estimating Large Pool Fire Burning Rates," *Fire Technology*, Vol. 19, Issue 4, November 1983, pp. 251-261.

16. Gritzo, L.A. and Boucheron, E.A., "Fuel Temperature Distribution and Burning Rate in Large Pool Fires," *Proposed for Presentation at the Annual Conference on Fire Research*, Gaithersburg, Maryland, October 28-31, 1996.

17. Schneider, M.E. and Kent, L.A., "Measurements of Gas Velocities and Temperatures in a Large Open Pool Fire," *Fire Technology*, Vol. 25, Issue 1, February 1989, pp. 51-80.

18. Koseki, H., "Combustion Properties of Large Liquid Pool Fires," *Fire Technology*, Vol. 25, Issue 3, August 1989, pp. 241-255.

19. Koseki, H., "Radiation Properties and Flame Structure of Large Hydrocarbon Pool Fires," *Thirteenth Meeting of the UJNR Panel on Fire Research and Safety*, Vol. 2, March 13-20, 1996.

20. Munoz, M., Arnaldos, J., Casal, J, and Planas, E., "Analysis of the Geometric and Radiative Characteristics of Hydrocarbon Pool Fires," *Combustion and Flame*, Vol. 139, Issue 3, November 2004, pp. 263-277.

21. Chatris, J.M., Quintela, J., Folch, J., Planas, E. Arnaldos, J., and Casal, J., "Experimental Study of Burning Rate in Hydrocarbon Pool Fire," *Combustion and Flame*, Vol. 126 Issues 1-2, July 2001, pp. 1373-1383.

22. Planas-Cuchi, E., Chatris, J.M., Lopez, C., and Arnaldos, J., "Determination of Flame Emissivity in Hydrocarbon Pool Fires Using Infrared Tomography," *Fire Technology*, Vol. 39, Issue 3, July 2003, pp. 261-273.

23. Klassen, M. and Gore, J.P., "Structure and Radiation Properties of Pool Fires," National Institute of Standards and Technology (NIST) Report, NISTIR-GCR-94-651, June 1994, Gaithersburg, Maryland.

24. Gritzo, L.A., Sivathanu, Y.R., and Gill, W., "Transient Measurements of Radiative Properties, Soot Volume Fraction and Soot Temperature in a Large Fire," *Combustion Science and Technology*, Vol. 139, Issue 1, August 1998, pp. 113-136.

25. Murphy, J.J. and Shaddix, C., "Soot Properties and Species Measurements in a Two-Meter JP-8 Pool Fire," Sandia Report SAND2003-8246, June 2003.

26. Jenson, K.A., Suo-Anttila, J., and Blevins, L.G., "Characterization of Soot Properties in Two-Meter JP-8 Pool Fire," Sandia Report SAND2005-0337, January 2005.

27. Kramer, M.A., Greiner, M., Koski, J.A., Lopez, C., and Suo-Anttila, A., "Measurements of Heat Transfer to a Massive Cylindrical Calorimeter Engulfed in a Circular Pool Fire," *Journal of Heat Transfer*, Vol. 125, February 2003, pp. 110-117.

28. Are, N., Greiner, M., Lopez, C., and Suo-Anttila, A., "Effect of Small Long-Duration Fires on a Spent Nuclear Fuel Transportation Package," *Institute of Nuclear Materials Management 45th Annual Meeting*, July 18-22, 2004, Orlando, Florida.

29. Koski, J.A., Gill, W., Gritzo, L.A., Kent, A., and Wix, S.D.), "Characterization of Indoor and Outdoor Pool Fires With Active Calorimetry," Sandia Report SAND94-2643C, August 6-8, 1995.

30. Mansfield, J.A., Gritzo, L., and Murray, D., "Test Report for Mock Fuselage Fire Test MF-8," Naval Air Warfare Center Weapons Division (NAWCWPNS) TP 8280, July 1996.

31. Gritzo, L.A., Moya, J.L., and Murray, D., "Fire Characterization and Object Thermal Response for a Large Flat Plate Adjacent to a Large JP-4 Fuel Fire," Sandia Report SAND97-0047, January 1997.

32. Gritzo, L.A. and Suo-Anttila, J.M., "Thermal Measurements for a JP-8 Pool Fire in Cross-Flow with a C-141 Fuselage Section Located on the Leeward Edge," Sandia Report SAND2001-0313, April 2001.

33. Gritzo, L.A. and Suo-Anttila, J.M., "Thermal Measurements From a Series of Tests With a Large Cylindrical Calorimeter on the Leeward Edge of a JP-8 Pool Fire in Cross-Flow," Sandia Report SAND2001-1986, July 2001.

34. Tieszen, S., "Time and Length Scales Within a Fire and Implications for Numerical Simulation," Sandia Report SAND2000-0320C, February 2, 2000.

35. Yeoh, G.H. and Yuen, K.K., *Computational Fluid Dynamics in Fire Engineering, Theory, Modelling and Practice*, Elsevier, Inc., Burlington, Massachusetts, 2009.

36. Ma, T.G. and Quintiere, J.G., "Numerical Simulation of an Axi-Symmetric Fire Plume: Accuracy and Limitations," *Fire Safety Journal*, Vol. 38, Issue 5, September 2003, pp. 467-492.

37. Li, J. Li, Y., Chow, W.K., and Huang, H., "Numerical Studies on Fire-Induced Thermal Plumes," *Journal of Thermal Sciences*, Vol. 14 Issue 4, December 2005, pp. 374-381.

38. Greiner, M. and Suo-Anttila, A., "Fast Running Pool Fire Computer Code for Risk Assessment Calculations," *Proceedings of 2003 IMECE: International Mechanical Engineering Congress and Exhibition*, November 15-21, 2003, Washington, DC.

39. Munoz, M., Planas, E., Ferrero, F, and Casal, J., "Predicting the Emissive Power of Hydrocarbon Pool Fires," *Journal of Hazardous Materials*, Vol. 144, Issue 3 June 18, 2007, pp. 725-729.

40. De Ris, J., "A Stochastic Combustion Model for Fire Plumes," *Fire Safety Journal*, Vol. 3, Issue 4, March 1981, pp. 287-297.

41. Official Website, "Fire Dynamics Simulator and Smokeview (FDS-SMV)," National Institute of Standards and Technology (NIST), Reviewed February 2011, http://www.fire.nist.gov/fds/index.html

42. Official Website, "The University of Utah: Center for the Simulation of Accidental Fires and Explosions (CSAFE), A DoE Advanced Simulation and Computing Center," University of Utah, Reviewed February 2011, http://www.csafe.utah.edu/publications.php

43. Spinti, J., Thornock, J.N., Eddings, E.G., Smith, P.J., and Sarofim, A.F., "Heat Transfer to Objects in Pool Fires," *Transport Phenomena in Fires*, Faghri, M. and Sundén, B., eds., *Development in Heat Transfer Series*, Vol. 20, WITPress, Southampton, U.K., 2008.

44. Guilkey, J.E., Harman, T.B., and Banerjee, B., "An Eulerian-Lagrangian Approach for Simulating Explosions of Energetic Devices," *Computers and Structures*, Vol. 85, January 2007, pp. 660-674.

45. Luitjens, J., Worthen, B., Berzins, M., and Henderson, T. (2007), "Scalable Parallel AMR for the Uintah Multi-Physics Code," *Petascale Computing: Algorithms and Applications*, Chapman and Hall/CRC, 2007.

46. Munson, B.R., Young, D.F., and Okishi, T.H., *Fundamentals of Fluid Mechanics*, *Fifth Edition*, John Wiley & Sons, Inc., Danvers, Massachusetts, 2006

47. Pope, S.B., *Turbulent Flows*, Cambridge University Press, Cambridge, U.K., (2000).

48. ANSYS, Inc. (2009), "ANSYS Fluent 12 Theory Guide," Reviewed February 2010, Printed April 2009, https://www.sharcnet.ca/Software/Fluent12/html/th/node3.htm

49. Raithby, G.D. and Chui, E.H., "A Finite-Volume Method for Predicting Radiant Heat Transfer in Enclosures with Participating Media," *Journal of Heat Transfer*, Vol. 112, May 1990, pp. 415-423.

50. Brookes, S.J. and Moss, J.B., "Prediction of Soot and Thermal Radiation in Confined Turbulent Jet Diffusion Flames," *Combustion and Flame*, Vol. 116, Issue 4, March 1999, pp. 486-503.

51. Boeing Commercial Airplanes (1968), "707 Airplane Characteristics Airport Planning," 707 Document D6-58322, Reviewed May 2011, http://www.boeing.com/commercial/airports/acaps707.pdf

52. Boeing Commercial Airplanes (1998), "777-200/300 Airplane Characteristics Airport Planning," 777 Document D6-58329, Reviewed May 2011, http://www.boeing.com/commercial/airports/acaps777_32.pdf

53. Airbus, "A380 Aircraft Characteristics Airport and Maintenance Planning AC," March 30, 2005 (revised November 1, 2012) Reviewed May 2011, http://www.airbus.com/fileadmin/media_gallery/files/tech_data/AC/AC_A380_2010101.pdf